Development of a one-dimensional model for the stability analysis of a natural circulation Super Critical Water Reactor

F.A.L. Kam

PNR-131-2011-007

M.Sc. Thesis

Supervisors: Dr. ir. M. Rohde
Dr. ir. C. T'Joen

Dept. of Radiation, Radionuclides & Reactors
Sect. Physics of Nuclear Reactors
Faculty of Applied Sciences
Delft University of Technology

Delft, June 2011

Committee members: Dr. ir. M. Rohde
Dr. ir. C. T'Joen
Dr. dipl.-ing. S. Kenjeres
Dr. ir. J. L. Kloosterman

Abstract

This report is written as part of the graduation project concluding the Master Applied Physics at the Delft University of Technology. The research described in this thesis was conducted at the section Physics of Nuclear Reactors of the Radiation, Radionuclides & Reactors department. It deals with analysis of the coupled thermal hydraulic-neutronic stability of a scaled facility, which mimics the physics of a natural circulation supercritical water reactor (SCWR). The SCWR is a Generation IV concept design, with an improved thermal efficiency. Strong density changes of the coolant across the reactor core can be used to drive the flow; this natural circulation increases the inherent safety. However, such naturally circulating flows can be prone to instabilities. The natural circulating HPLWR is a SCWR design proposal. To investigate its stability, an experimental facility representing the HPLWR was designed using a scaling fluid (R23).

As a part of this MSc project, a computational tool which uses a transient analysis technique was developed in order to numerically investigate the stability. A description of the equations governing the flow and the solution algorithm used in the code are presented in this thesis and the experimental set-up is described. A comparison is made between experimental and numerical steady state mass flow rates. For a variety of operating conditions, limited by the experimental set-up, an experimental power-flow map was successfully reproduced with the code. The numerical stability predictions and the stability of the experimental facility are compared as well, showing good agreement.

Comparison of experimental and numerical studies of parametric effects show more mixed results. The effect of a lower fuel constant differs significantly when experiments are compared to numerical predictions, other effects show good agreement.

It is recommended to perform a temporal- and spatial grid refinement study at high N_{p-pch} values, in order to numerically investigate the stability of a larger section of the N_{p-sub}-N_{p-pch} plane. A study regarding parametric effects should be extended over the N_{p-sub}-N_{p-pch} plane as well. Furthermore, by using the correct HPLWR neutronic parameters, results can be scaled up to the HPLWR for comparison. It might also be possible to improve the computational speed of the code by eliminating calls to the NIST [Huber et al. (2002)] thermo-dynamic properties package. The accuracy of the code might benefit from adapting the 'buffer vessel' to eliminate mass in- and outflow after reaching the desired steady state flow rate.

Samenvatting

Dit verslag maakt onderdeel uit van het eindproject van de studie Technische Natuurkunde van de Technische Universiteit Delft. Het onderzoek dat beschreven wordt in dit verslag is uitgevoerd bij de sectie Physics of Nuclear Reactors van de vakgroep Radiation, Radionuclides & Reactors. Het behandelt onderzoek naar de thermo hydraulisch-neutronisch gekoppelde stabiliteit van een geschaalde opstelling, die de natuurkunde van een natuurlijke circulatie superkritisch water reactor (SCWR) nabootst. De SCWR is een generatie IV concept ontwerp, met een hogere thermische efficiëntie. Het grote dichtheidsverschil in de reactorkern kan gebruikt worden om stroming van de koelvloeistof in stand te houden; deze natuurlijke circulatie is inherent veiliger. Dergelijke natuurlijke circulatie stromingen zijn echter gevoelig voor instabiliteiten. De natuurlijke circulatie HPLWR is een voorstel voor een SCWR ontwerp. Een experimentele opstelling die de natuurkunde van de HPLWR nabootst, is ontworpen met behulp van een schaalvloeistof (R23) om de stabiliteit ervan te onderzoeken.

Als onderdeel van dit MSc project is een code ontwikkeld, waarin een transiënte analyse techniek gebruikt wordt om de stabiliteit van zo'n geschaalde opstelling numeriek te onderzoeken. In dit verslag worden de vergelijkingen die de koelvloeistofstroming beschrijven en het oplossings-algoritme gepresenteerd en de experimentele opstelling wordt beschreven. Er wordt een vergelijking gemaakt tussen experimentele en numerieke steady state massa-stromen. Een experimentele power-flow curve is succesvol gereproduceerd met de code voor verschillende condities, beperkt door de experimentele opstelling. De numerieke stabiliteitsvoorspellingen en de stabiliteit van de opstelling zijn ook vergeleken en vertonen een sterke overeenkomst.

Er is met wisselend succes een vergelijking gemaakt tussen experimentele en numerieke parameter studies. Het effect van het verlagen van de brandstof constante verschilt significant tussen experimenten en simulaties, andere effecten komen overeen.

Het is aan te raden een grid-afhankelijkheidsanalyse te doen bij hoge N_{p-pch} waarden. Hierdoor kan de stabiliteit in een groter deel van het N_{p-sub}-N_{p-pch} vlak onderzocht worden. Het onderzoek naar parametrische effecten kan ook uitgebreid worden, door het N_{p-sub}-N_{p-pch} vlak te bekijken en door meer parameters te onderzoeken. Verder kunnen verkregen resultaten opgeschaald worden voor vergelijking met de HPLWR, indien de juiste HPLWR neutronica parameters gebruikt worden. De snelheid van de code zou sterk verbeterd kunnen worden door het aanroepen van het NIST [Huber et al. (2002)] thermo-dynamische eigenschappen pakket te vermijden. De nauwkeurigheid van de code zou kunnen verbeteren door het aanpassen van het ‘buffer vat’, door het uitsluiten van massa in- en uitstroom na het bereiken van de gewenste steady state massa-stroomsnelheid.

Contents

Abstract **v**

Samenvatting **vii**

1 Introduction **1**

2 Theory **5**

2.1 Thermal hydraulics 5

2.2 Thermal hydraulic-neutronic coupling 10

2.3 Flow instabilities 15

3 Numerical Scheme **19**

3.1 Introduction 19

3.2 Buffer vessel 19

3.3 Discretization 20

3.4 Algorithm 22

3.4.1 Pressure correction 24

3.4.2 Neutronic feedback implementation 25

3.4.3 Solving the system of equations 27

3.4.4 Overview of the solution algorithm 28

4 Experimental facility **29**

4.1 Downscaling the HPLWR 29

4.2 DeLight facility 29

4.3 Experimental procedure 32

5 Results **35**

5.1 Benchmarking 35

5.1.1 Comparison of power-flow map with literature 35

5.1.2 Power-flow map of the DeLight facility 37

5.1.3 Obtaining the correct steady state conditions 38

5.2 Convergence 41

5.3 Experimental stability map 45

5.4 Parametric effects on stability 47
5.4.1 Effect of inlet- and outlet friction at the core 47
5.4.2 Effect of a uniform power profile 48
5.4.3 Effect of moderator rods 50
5.4.4 Effect of the fuel constant 52

6 Conclusions & Outlook **55**
6.1 Conclusions 55
6.2 Outlook 56

A Flow obstruction constants **59**

B Scaling factors **61**

List of figures **65**

Bibliography **67**

Nomenclature **69**

Chapter 1

Introduction

Nuclear experts around the world are investigating the possibility to design a new type of nuclear power plant that will improve safety, proliferation resistance and minimizes natural resource utilization and the production of radioactive waste. Furthermore, the objective is to decrease the costs to build and operate such a plant. In 2001 Argentina, Brazil, Canada, France, Japan, the Republic of Korea, the Republic of South Africa, the United Kingdom and the United States founded the Generation IV International Forum with the objective of identifying and evaluating the most promising nuclear energy technologies of the next generation.

One of the selected fourth generation concepts is the supercritical water reactor (SCWR). This is a light water reactor where the coolant flows under supercritical conditions. A fluid at a pressure and temperature higher than its critical point is called supercritical. For water this critical point is at a temperature of 373.9 ^{0}C and pressure of 220.6 bar. Because under supercritical conditions the coolant does not undergo a phase change, a higher core outlet temperature, and thus a higher thermal efficiency, can be reached with a SCWR compared to an ordinary boiling water reactor (BWR) or pressurized water reactor (PWR). Furthermore, the SCWR design is simplified and more compact because it does not incorporate steam-water separation and recirculation pumps and only consists of one coolant loop.

One specific design proposal for a SCWR is called the high performance light water reactor (HPLWR). Its critical scientific issues and technical feasibility are investigated by a consortium consisting of ten partners from eight European countries under supervision of the European Commission. The HPLWR is projected to have a thermal efficiency of approximately 45%, which is a significant improvement compared to current deployed BWR's and PWR's that have thermal efficiencies near 35%. In the design proposal of the HPLWR no definitive choice has been made between forced circulation by a pump versus natural circulation of the coolant. The latter has the advantage that it is inherently safer.

At the designed system pressure of 250 bar, the coolant (water) is well above its critical pressure. Since the coolant temperature is increased in the core from 280 ^{0}C to 500 ^{0}C, the flow conditions change from sub- to supercritical. It was found that heating up the coolant in one single step would result in local temperatures exceeding the design limits of the core internals. [Schulenberg et al. (2008)] This is highly unwanted since it may result in failure of the fuel cladding and contamination of the coolant. To overcome this problem the coolant is heated in three stages in the HPLWR core. Between the different heating stages, mixing zones ensure a more homogeneous radial distribution of enthalpy, preventing the occurrence of local hot spots. Another outstanding feature in the HPLWR three-pass core design is the use of water rods for moderation of neutrons.

Experience has shown that coolant flow instabilities do occur in boiling water reactors due to the large range of densities present in the core. [March-Leuba and Rey (1993)] These densities range from 740 kg/m^3 in the lower plenum to 180 kg/m^3 in the upper plenum. In the design proposal for the HPLWR, the difference in densities across the reactor core is even larger, ranging from 777 kg/m^3 to 90 kg/m^3. This is expected to result in similar stability issues for the HPLWR.

The stability of the HPLWR is studied numerically by, among others, Ortega Gomez (2009), but an experimental study involving an actual physical system might provide more accurate results. The costs of such an experimental study can be greatly reduced by downscaling the HPLWR design to smaller dimensions, lower pressures, lower temperatures and a lower power using a specific scaling fluid different from water. The scaling rules and scaling fluid are found in Rohde et al. (2011). This work has resulted in an experimental facility, named DeLight, mimicking the coolant flow of the HPLWR, with natural circulation of the coolant throughout the system. A schematic representation of the DeLight facility is given in figure 1.1. In an experimental facility, however, it can be difficult or even impossible to control or change certain parameters during experiments. Therefore a numerical study of the facility combined with actual experiments at the facility promises to capture all of the advantages.

The first goal of the research conducted for this master thesis is to develop a one-dimensional code, able to simulate the dynamic behaviour of the DeLight facility. In accordance with the vast amount of time it took to develop this code during the project, it is treated quite extensively in this thesis. The results from the code will be benchmarked with experimental steady state data and with steady state data from a supercritical loop with a different geometry and cooling liquid found in literature [Jain and Rizwan-uddin (2008)]. Secondly a stability analysis will be made with the developed code and the results will be compared to the results from the stability analysis on the DeLight facility. Finally, performing a parametric study with the code provides a more cost-effective way to research improvements of the design of the DeLight facility and/or the HPLWR.

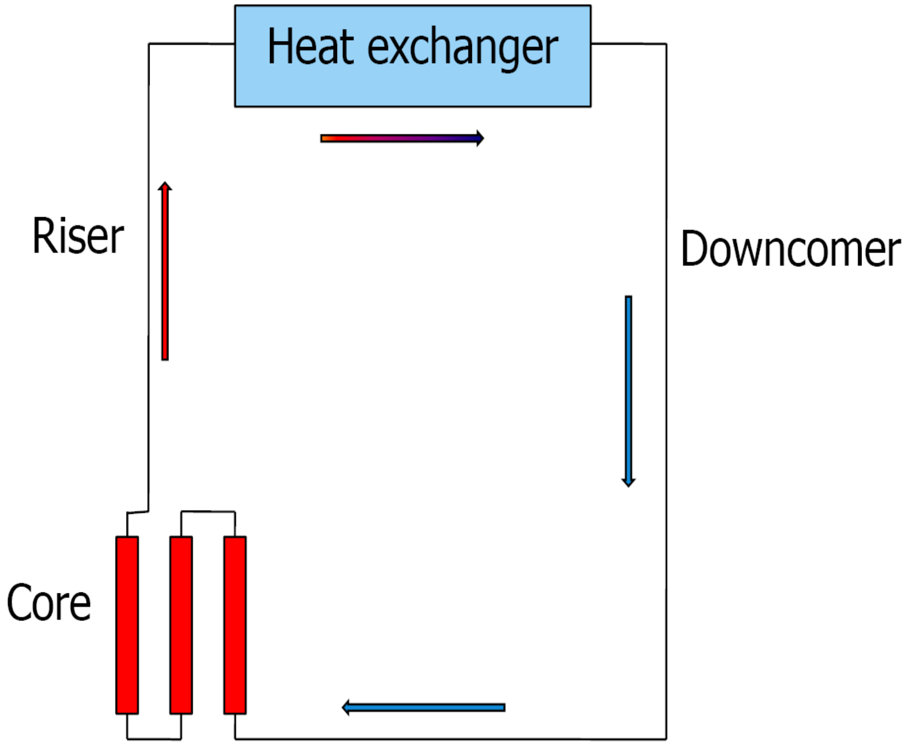

Figure 1.1: A simplified illustration of the DeLight facility.

Similar work was carried out earlier for the economic simplified boiling water reactor (ESBWR), with a downscaled experimental facility and a code [Marcel (2007)]. For the same facility a one-dimensional code, named STEALTH, was developed. This code was reported to have some shortcomings resulting in an inaccurate power flow map [Koopman (2008)]. But since these problems seemed specific for the simulation of two-phase flow, the code was found to be promising for the simulation of the supercritical (one-phase) flow in the DeLight facility. The system of equations used in the STEALTH code is adapted for supercritical conditions and the geometry is modified as well to the specifications of the DeLight facility (and separately for the geometry described by Jain and Rizwan-uddin (2008)). Furthermore, a coolant density reactivity feedback effect is incorporated into the code that describes the DeLight facility, because it is expected to have a significant effect on the stability of the system as shown for the forced-circulation driven HPLWR by Ortega Gomez (2009).

Chapter 2

Theory

2.1 Thermal hydraulics

The motion of fluids is governed by the transport of mass, momentum and energy. The continuity equation (eq. 2.1) describes the conservation of mass, the momentum balance equation (eq. 2.2) describes the conservation of momentum and the energy balance equation (eq. 2.3) describes the conservation of energy. These equations describe the flow and are known as the Navier-Stokes equations.

$$\frac{\partial \rho}{\partial t} + \nabla \cdot (\rho \vec{v}) = 0 \tag{2.1}$$

$$\frac{\partial (\rho \vec{v})}{\partial t} + \nabla \cdot \rho \vec{v}\vec{v} = -\nabla p + \nabla \cdot \vec{\tau} + \rho g \tag{2.2}$$

$$\frac{\partial (\rho u^0)}{\partial t} + \nabla \cdot \rho u^0 \vec{v} = -\nabla \cdot \vec{q}'' + Q + \nabla \cdot p\vec{v} + \nabla \cdot (\vec{\tau} \cdot \vec{v}) + \vec{v} \cdot \rho g \tag{2.3}$$

Since the system of interest is one-dimensional, an integration is carried out over the cross-sectional area perpendicular to the direction of flow. Integrating equation 2.1 over a control volume and employing Gauss's Divergence theorem [Stewart (1999)] gives:

$$\iiint\limits_V \frac{\partial \rho}{\partial t} dV + \iiint\limits_V \nabla \cdot (\rho \vec{v}) dV = V \frac{\partial \bar{\rho}}{\partial t} + \iint\limits_A (\rho \vec{v}) \cdot dA = 0 \tag{2.4}$$

In a one-dimensional system ρ and $\vec{v}$ are constant over the cross-sectional area, so the averaging operator on ρ can be dropped and $\vec{v}$ will only have a non-zero component, v_x, in the x-direction, which is the direction of flow. The infinitesimal limit can be taken of the width in the flow direction of the control volume, Δx, and it can be divided out of equation 2.4:

$$A\frac{\partial \rho}{\partial t} + \lim_{x\to 0}\frac{[A\rho v_x]_x^{x+\Delta x}}{\Delta x} = A\frac{\partial \rho}{\partial t} + \frac{\partial M}{\partial x} = 0 \tag{2.5}$$

In a similar manner an expression for the momentum balance equation can be found:

$$A\frac{\partial(\rho v_x)}{\partial t} + \frac{\partial}{\partial x}(A\rho v_x^2) = -A\frac{\partial p}{\partial x} - \oint_{P_w} \tau_w dP_w + \rho g A \tag{2.6}$$

The friction due to the wall perimeter, P_w, includes not only the outer perimeter of the tubing, but also any obstacle in the flow path with a length in the direction of flow. Therefore the integral over τ_w runs along the cross-sectional area of every obstacle. With the definition of the hydraulic diameter and the relation for the wall friction as proposed by Darcy, described in Kazimi and Todreas (1990);

$$D_h = \frac{4A}{P_w} \tag{2.7}$$

$$\oint_{P_w} \tau_w dP_w = \tilde{\tau}_w P_w = f\frac{M^2}{2D_h A\rho} \tag{2.8}$$

and by inserting equations 2.7 and 2.8 in 2.6, the one-dimensional momentum balance equation becomes:

$$\frac{\partial M}{\partial t} + \frac{\partial}{\partial x}\left(\frac{M^2}{A\rho}\right) = -A\frac{\partial p}{\partial x} - f\frac{P_w M^2}{8A^2\rho} + \rho g A \tag{2.9}$$

Employing the same strategy as before the one-dimensional energy balance equation can be rewritten. Because there is no internal heat generation and shear and gravitational effects on friction are negligible, equation 2.3 can be simplified to:

$$A\frac{\partial \rho u^0}{\partial t} - \frac{\partial}{\partial x}A\rho v_x\left(u^0 + \frac{p}{\rho}\right) = q' \tag{2.10}$$

Where the part in brackets is identified as the enthalpy and since it is much easier to keep track of numerically, the choice to work with enthalpy instead of internal energy becomes clear. Furthermore, the kinetic energy may be neglected [Kazimi and Todreas

(1990)] to obtain the following one-dimensional enthalpy balance equation in which a time-dependent pressure term is present:

$$A\frac{\partial \rho h}{\partial t} + \frac{\partial M h}{\partial x} = q' + A\frac{\partial p}{\partial t} \tag{2.11}$$

So far some quantities are still unknown and they have to be specified to complete the system of equations. The assumption that the external power is transferred instantaneously from the fuel into the coolant in the core-sections and from the coolant in the heat exchanger, gives a linear heating rate in the core sections

$$q'_C = \frac{P}{L_{heated}} \tag{2.12}$$

and in the heat exchanger

$$q'_{HX} = -\frac{P}{L_{cooled}} \tag{2.13}$$

It is assumed that in all other parts of the system no heat is exchanged with the environment.

The dynamic viscosity, μ, of the coolant is computed from a series of splines that depend on the enthalpy over the interval of interest. The series of splines is determined from data points from the thermodynamic properties package NIST. [Huber et al. (2002)] Special care was taken to capture the sharp change at the pseudo critical point, by concentrating the data points more near this point as shown in figure 2.1.

Furthermore, an equation of state for the density as a function of pressure and temperature $\rho = \rho(p, T)$ is to be provided. A first order Taylor expansion of the density in terms of temperature and pressure results in the following equation to calculate the change in density:

$$d\rho = \left[\frac{\partial \rho}{\partial T}\right]_p dT + \left[\frac{\partial \rho}{\partial p}\right]_T dp \tag{2.14}$$

The partial derivatives of ρ in equation 2.14 can be called from the NIST [Huber et al. (2002)] properties package. As this is of a numerical nature, it will be explained in chapter 3.

The friction factor f, mentioned before, still has to be defined. It is common to describe this friction factor as a function of the Reynolds number [Kazimi and Todreas (1990)]:

$$Re = \frac{\rho|\vec{v}|D_h}{\mu} = \frac{|M|D_h}{A\mu} \tag{2.15}$$

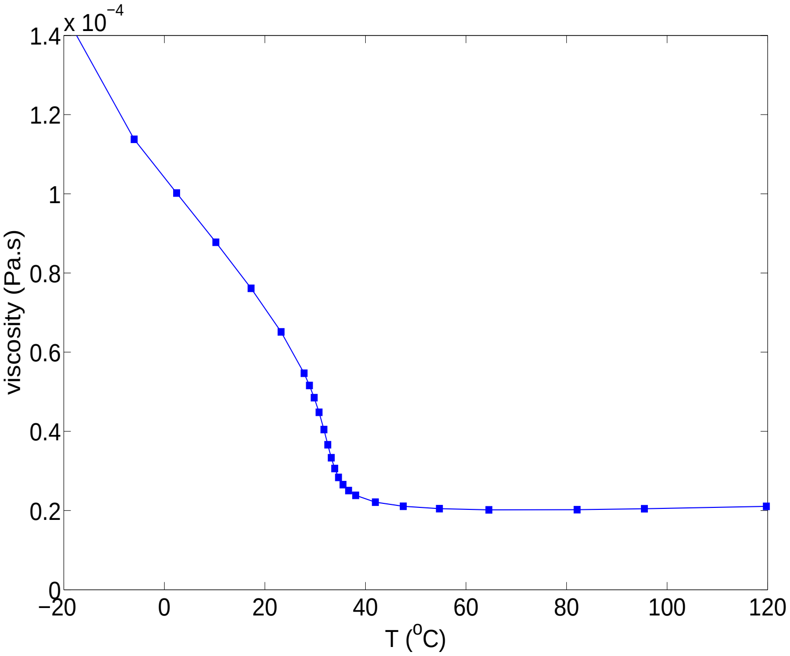

Figure 2.1: Concentration of data points at pseudo critical point to capture the sharp change in viscosity.

$$f = \begin{cases} 0 & \text{if } Re < 10^{-3} \\ \frac{64}{Re} & \text{if } 10^{-3} \leq Re < 2.1 \cdot 10^{3} \\ 0.316 Re^{-0.25} & \text{if } 2.1 \cdot 10^{3} \leq Re < 3 \cdot 10^{4} \\ 0.184 Re^{-0.2} & \text{if } 3 \cdot 10^{4} \leq Re < 4 \cdot 10^{4} \\ \frac{1}{(-1.8 \log[\frac{6.9}{Re} + (\frac{\epsilon/D_h}{3.7})^{10/9}])^2} & \text{if } Re \geq 4 \cdot 10^{4} \end{cases} \tag{2.16}$$

The last relation (for high Reynolds numbers) is known as the Haaland equation and can be found in Haaland (1983). Apart from the warming up period of the supercritical system, the Haaland equation is predominantly used in the simulations. With equations 2.8, 2.15 and 2.16 it is possible to calculate the wall friction induced by the straight tubes of the system. However, the DeLight facility does not merely consist of straight tubes, but also has bends, corners and other elements obstructing the flow. These obstructions are incorporated into the momentum balance equation. This is done in the form of a local pressure loss term, Δp_i. The integral over the cross-sectional area of the gradient of p becomes:

$$\begin{aligned}\iint_A \nabla \left(p + \sum_i \Delta p_i H_{step}(x_i) \right) dA &= A \frac{\partial}{\partial x} \left(p + \sum_i \Delta p_i H_{step}(x_i) \right) \\ &= A \frac{\partial p}{\partial x} + A \sum_i \Delta p_i \delta(x - x_i) \end{aligned} \tag{2.17}$$

The pressure loss term in the above equation is described as:

$$\Delta p_i = C_v \left(\frac{A_i}{A} \right)^2 \frac{M^2}{2A^2 \rho} = K_i \frac{M^2}{2A^2 \rho} \tag{2.18}$$

With an empirically found friction coefficient, K_i, as described in appendix A [Kazimi and Todreas (1990), Janssen and Warmoeskerken (2006)]. The one-dimensional momentum balance equation including the flow obstructions becomes:

$$\frac{\partial M}{\partial t} + \frac{\partial}{\partial x} \left(\frac{M^2}{A\rho} \right) = -A \frac{\partial p}{\partial x} - \sum_i K_i \frac{M^2}{2A\rho} \delta(x - x_i) - f \frac{P_w M^2}{8A^2 \rho} + \rho g A \tag{2.19}$$

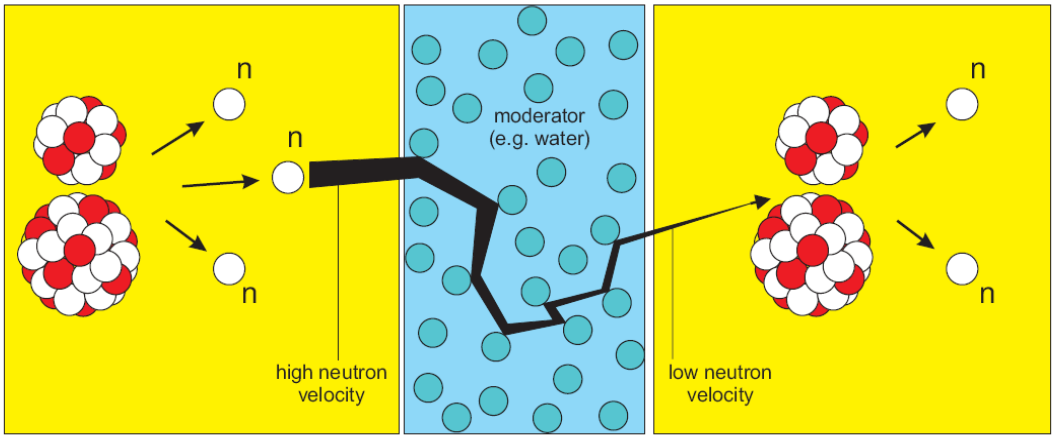

Figure 2.2: A schematic representation of fission of uranium-235 and moderation of neutrons. [figure from Ortega Gomez (2009)]

2.2 Thermal hydraulic-neutronic coupling

In the design of the HPLWR power generation occurs via the fission of uranium into lighter elements. A thermal (slow) neutron colliding with an uranium-235 atom has a relatively high probability of inducing a fission reaction, releasing high velocity neutrons. Because the probability of absorption of these fast neutrons by uranium atoms is rather low, the high velocity neutrons must be slowed down by a moderator to maintain the chain reaction depicted in figure 2.2. The fission rate and subsequently the heat generated in a reactor core by these fission reactions are directly correlated to the thermal neutron density, $n(t)$. The instantaneous volumetric heat generation in the fuel is given by:

$$q''' = w_f \Sigma_f n(t) v_n \tag{2.20}$$

With w_f, the energy released per fission, Σ_f, the macroscopic cross-section of a fission event and v_n the velocity of the neutron.

The reactor dynamics can, in a simplified form, be represented by the point-kinetic equations [Duderstadt and Hamilton (1976)]. In this model the spatial dependence of the neutron flux, $\Phi(\vec{r}, t)$, is assumed to consist of one fundamental mode, $\Psi(\vec{r})$. The following separation ansatz for space and time is applied:

$$\Phi(\vec{r}, t) = n(t) v_n \Psi(\vec{r}) \tag{2.21}$$

$$C_i(\vec{r}, t) = C_i \Psi(\vec{r}), \tag{2.22}$$

where C_i are the concentrations of delayed neutron precursors. Although most of the fission neutrons appear promptly after the fission event, a small fraction β (approximately 0.65%) is emitted with a substantial time delay. These delayed neutrons can be divided in six groups, and for each group a concentration balance equation is formulated by the change of the concentration C_i, the fraction β_i of generated delayed neutrons and the reduction given by the decay constant λ_i of the specific group (equation 2.25). Naturally the sum of the fractions of each delayed neutron group equals the total fraction of delayed neutrons:

$$\beta = \sum_{i=1}^{6} \beta_i. \tag{2.23}$$

The time evolution of the neutron density and precursor concentrations can in turn be described by:

$$\frac{dn}{dt} = \frac{\rho_{reactivity} - \beta}{\Lambda_{gen}} n(t) + \sum_{i=1}^{6} \lambda_i C_i(t) \tag{2.24}$$

$$\frac{dC_i}{dt} = \frac{\beta_i}{\Lambda_{gen}} n(t) - \lambda_i C_i(t), \quad i = 1, ..., 6 \tag{2.25}$$

This set of seven coupled ordinary differential equations describes the change in the neutron population and the decay of the delayed neutron precursors. The delayed neutrons generated in earlier generations are additional source terms in equation 2.24. The reactivity, $\rho_{reactivity}$, is defined as the deviation of the multiplication factor, k, from the critical value ($k = 1$) over the multiplication factor. It gives the fraction of new generated neutrons of the total neutron population during the mean life time of one neutron generation, Λ_{gen}.

$$\rho_{reactivity} = \frac{k-1}{k} \tag{2.26}$$

The mean generation time is defined as the lifetime of prompt neutrons, l, divided by the multiplication factor.

$$\Lambda_{gen} = \frac{l}{k} \tag{2.27}$$

With exception of the mean neutron generation time (scaled from a BWR), the parameters of the point-kinetics model are scaled from the parameters of the HPLWR listed in Ortega Gomez (2009) according to the scaling rules described in Rohde et al. (2011) and are listed in table 2.2.

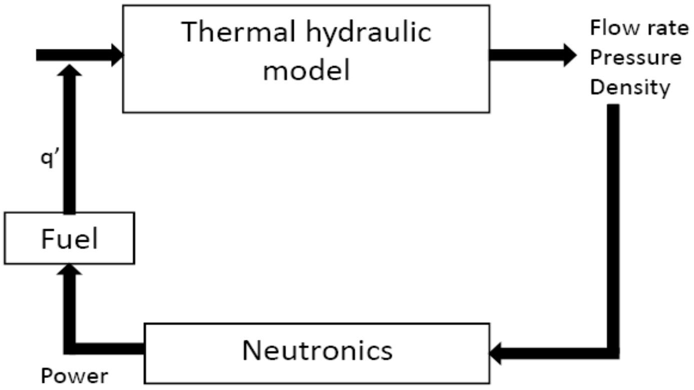

Figure 2.3: A schematic representation of the coolant density feedback mechanism.

Table 2.2: Parameters of the point-kinetics model for DeLight.

Fraction		Decay constant	
β_1	0.038β	λ_1	0.0290 s^{-1}
β_2	0.213β	λ_2	0.0724 s^{-1}
β_3	0.188β	λ_3	0.263 s^{-1}
β_4	0.407β	λ_4	0.710 s^{-1}
β_5	0.128β	λ_5	3.20 s^{-1}
β_6	0.026β	λ_6	8.84 s^{-1}
β	0.0065	Λ	22 μs

From equation 2.20 it is clear that the heat or power generated in a reactor core is directly proportional to the thermal neutron density, which in turn depends on the inserted reactivity as can be seen in equation 2.24. This inserted reactivity is correlated with the coolant density. Because the coolant acts as moderator to the fast neutrons (as depicted in figure 2.2) a change in coolant density will influence the amount of thermal neutrons available for fission reactions. In short: a change in coolant density changes the power generated in the core, which influences the coolant density. This results in a feedback mechanism as depicted in figure 2.3.

The density feedback coefficient of reactivity, $\alpha_{\rho_{coolant}}$, is defined as:

$$\alpha_{\rho_{coolant}} = \frac{\partial \rho_{reactivity}}{\partial \rho_{coolant}} \tag{2.28}$$

For the HPLWR it is parametrized for the appropriate coolant density range by Schlagenhaufer et al. (2007). From the scaling rules for the DeLight facility described in

Rohde et al. (2011) it follows that the scaling factor for the density coefficient of reactivity $X_{\alpha_{\rho_{coolant}}}$, equals the inverse density scaling factor $X^{-1}_{\rho_{coolant}}$ as can be seen in appendix B. So the density coefficient of reactivity for DeLight is given by:

$$\alpha_{\rho_{coolant}} = \frac{[-0.01424\rho_{coolant} + 0.04236]}{X_{\rho_{coolant}}} \tag{2.29}$$

With the coolant density, $\rho_{coolant}$, in (g/cm^3). During the simulations one fixed value for the density coefficient of reactivity is taken, $\alpha_{\rho_{coolant}} = 2.085\,\mathrm{cm^3/g}$. It should be noted that this coefficient has a positive value and it is interesting to point out the difference with a BWR. In a BWR, the void reactivity coefficient is negative. As such, an increase in void fraction, due to an increased reactivity, results in a decrease in reactivity via the void reactivity feedback effect. Since there's only one phase present in a SCWR, it is impossible to define a void fraction as in a BWR. Therefore, another coefficient is used to incorporate the effect of the drastic changes in the coolant properties at the critical point. From 2.28, it becomes clear that the density feedback coefficient of reactivity is used for the SCWR. This coefficient must be positive to ensure a decrease in reactivity as a result of a decrease in coolant density.

The heating sections in the DeLight facility provide an axially flat power profile. As such, only a change in the core averaged coolant density can influence the reactivity. Since the effect on the reactivity of a change in coolant density is independent of its axial position, the reactivity can be calculated with:

$$\rho_{reactivity} = \alpha_{\rho_{coolant}} \delta\rho_{coolant} \tag{2.30}$$

Where $\delta\rho_{coolant}$ is the deviation of the average coolant density in the core from the average coolant density in the core at steady state.

The coupled thermal hydraulic-neutronic feedback mechanism is computed as follows. From the coolant density, resulting from the thermal hydraulic model, the inserted reactivity is calculated with equation 2.30. This is used as input for the point-kinetics model to obtain a new value for the reactor power, as described below [Rohde (2010)]. The neutron density, the precursor concentrations and the reactivity can be expressed in terms of a steady state value and a perturbation:

$$n(t) = n_0 + n'(t) \tag{2.31}$$

$$C_i(t) = C_{i,0} + C_i'(t) \tag{2.32}$$

$$\rho_{reactivity}(t) = \rho'_{reactivity}(t) \tag{2.33}$$

The point-kinetic equations (eqs. 2.24 and 2.25) can be described in terms of these perturbations. From equations 2.20 and 2.31 it becomes clear that the perturbation of the power, p', from the steady state value (p_0), is directly proportional to the perturbation of the neutron density, n'. So the parameter of interest is actually the relative perturbation of the neutron density, defined as:

$$\underline{n}' \equiv n'/n_0 = \underline{p}' \equiv p'/p_0 \tag{2.34}$$

Combining equation 2.34 with $\underline{C}_i' \equiv C_i'/n_0$, equations 2.24 and 2.25 can be rewritten in terms of the relative perturbation:

$$\frac{d\underline{n}'}{dt} = \frac{\rho'_{reactivity}}{\Lambda_{gen}} + \underline{n}'\frac{\rho'_{reactivity}}{\Lambda_{gen}} - \underline{n}'\frac{\beta}{\Lambda_{gen}} + \sum_{i=1}^{6} \lambda_i \underline{C}_i'(t) \tag{2.35}$$

$$\frac{d\underline{C}_i'}{dt} = \frac{\beta_i}{\Lambda_{gen}}\underline{n}' - \lambda_i \underline{C}_i'(t), \quad i = 1, ..., 6 \tag{2.36}$$

Because it takes some time to transport heat from the fuel elements to the coolant, a power-transfer function, G_F, is introduced. It is assumed that this power-transfer function can be described by a first order process with one time-constant, τ.

$$\tau \frac{\partial}{\partial t'} q'_{extra} + q'_{extra} = P'(t) \tag{2.37}$$

With $P'(t')$, the step in power at $t' = 0$. Using $\underline{q}'_{extra} \equiv q'_{extra}/q'_0$, this differential equation can be discretized to

$$\left[1 + \frac{\tau}{\Delta t}\right] \underline{q}'_{extra}(n) - \frac{\tau}{\Delta t} \underline{q}'_{extra}(n-1) = P'(n), \tag{2.38}$$

which can be z-transformed. Because $P'(n) = \delta \underline{p}'(n)$, the transfer function in the z-domain becomes:

$$G_F(z) = \frac{\delta \underline{q}'^{n}_{extra}}{\delta \underline{p}'^{n}} = \frac{1}{b_1 + b_2 z^{-1}} \tag{2.39}$$

The constants, b_1 and b_2, are defined as:

$$b_1 = 1 + \frac{\tau}{\Delta t} \tag{2.40}$$

$$b_2 = -\frac{\tau}{\Delta t} \tag{2.41}$$

τ is related to the fuel rod diameter. It can be estimated from the heat balance in a circular rod [Van der Hagen (1988)]:

$$\tau = -\frac{c_p \rho_f V_f \Delta t}{q' A_f} \tag{2.42}$$

In a BWR the fuel constant τ is roughly around 4 to 6 seconds. With the power-transfer function, the extra power resulting from the coolant density feedback effect can be related to an extra linear heat rate, q'_{extra}, that must be added to the linear heat rate, q', of the reactor core in the enthalpy balance equation (eq. 2.11).

2.3 Flow instabilities

Super Critical Water Reactors are susceptible to system-wide flow instabilities, just as the widely used Boiling Water Reactors are. [Rohde et al. (2011), March-Leuba and Rey (1993)] In this section the physical mechanisms are described that can lead to flow instabilities. According to Boure et al. (1973), these instabilities can be classified into static- and dynamic instabilities. The static instabilities can be explained by the static or steady state characteristics of the thermal hydraulic system. The name is slightly misleading since the behaviour of the system is dynamic. These static instabilities are predicted by the analysis of the relation between the steady state pressure drop and flow rate. One example of a static instability is a Ledinegg instability [Boure et al. (1973)].

In the case of dynamic instabilities, knowledge of the steady state solutions of the system is not sufficient to predict the instability threshold. Because inertia and feedback mechanisms govern the dynamic instabilities, the stability boundaries must be found by analysis of the time-dependent characteristics of the system. The pressure drop oscillation (PDO) is a dynamic instability that can occur when a flow channel is connected to a pressure holder. It is the result of a feedback mechanism between a compressible volume and a thermal hydraulic channel, where the oscillations in the compressible volume and the channel are triggered by a flow excursion [Boure et al. (1973)].

Expected instabilities in SCWR's are density wave oscillations (DWO's), which are dynamic channel thermal hydraulic instabilities or coupled neutronic-thermal hydraulic instabilities. The latter are composed dynamic instabilities because they depend not only on the channel thermal hydraulics but also on a reactivity feedback effect. Both originate from the density wave oscillations that are governed by the inlet flow feedback mechanism. In a natural circulation BWR there are two distinct types of DWO's [Van Bragt (1998)]. First the Type-II DWO will be explained in more detail without the effect of neutronic feedback.

If the coolant flows upwards in a core section, local variations in density will be transported upwards. For example, when the inlet flow rate into the core is decreased, while

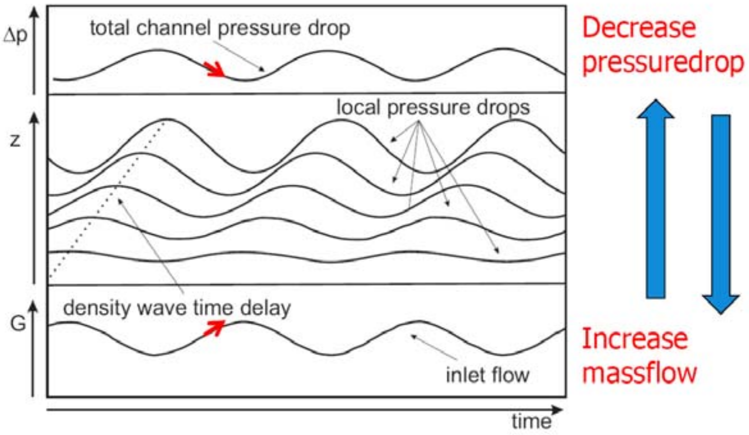

Figure 2.4: Illustration of the local pressure drop delay introduced by the density wave mechanism. [figure revision from March-Leuba and Rey (1993)]

the power is constant, a decrease in density will result. To evacuate the same amount of heat with a lower mass flow rate, the coolant needs to become warmer. This warmer packet of coolant has a lower density and it will travel upwards forming a density wave. At each axial location it produces a change in local pressure drop, delayed by the effective time for the lower density packet to move upwards through the core. If the inlet flow is perturbed sinusoidally as depicted in figure 2.4, the local pressure drops are also approximately sinusoidal. However, they are delayed with respect to the perturbation due to the travel time of the density wave. Therefore the total pressure drop across the channel is a sum of a delayed series of sinusoids and is also of a sinusoidal form, delayed with respect to the inlet flow perturbation. The total pressure drop can be delayed 180 degrees with respect to the perturbed inlet flow. When this occurs, an increase in inlet flow will result in a decrease of the channel pressure drop, what in turn results in an increase in inlet flow. (indicated by the red arrows in figure 2.4) In this case any inlet flow perturbation feeds on itself and oscillations will grow, thus the channel flow is unstable. These Type-II instabilities become important under high-power conditions [March-Leuba and Rey (1993), Van Bragt (1998)].

Type-I instabilities in a natural circulation BWR are gravitation driven and occur when the flow rate is much smaller than under the high-power Type-II conditions. In these circumstances, a small increase in core-outlet quality (χ), due to a decrease in inlet flow rate, results in a large increase of the void fraction (α) in the riser and, consequently, in a large change of the driving force of the flow. The time scale of Type-I oscillations is determined by the travel time of the two-phase mixture through the core and riser section, the time scale of Type-II oscillations by the travel time through the core. Type-I instabilities will therefore have a much smaller frequency than Type-II

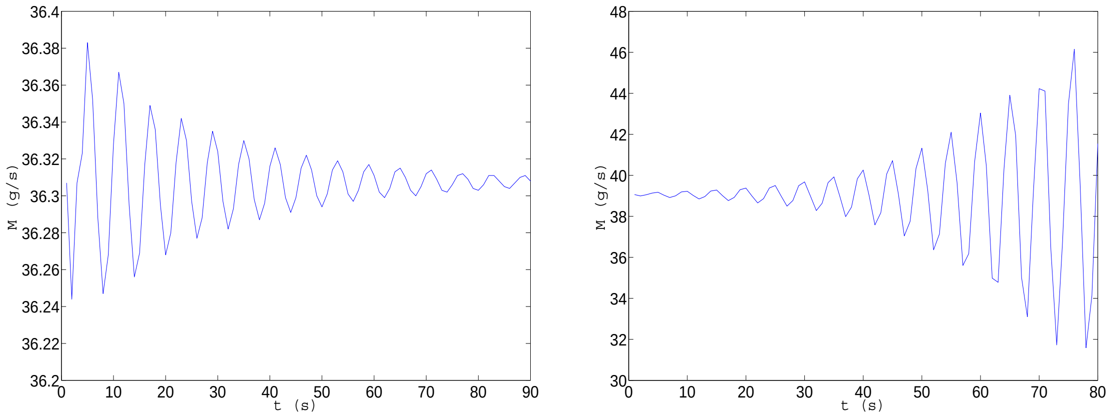

(a) *(b)*

Figure 2.5: Examples of a stable (a) and unstable (b) mass flow rate at the core inlet.

instabilities. In a natural circulation BWR typical frequencies are 0.2 Hz for Type-I and 0.6 Hz for Type-II instabilities. However, there's no sharp boundary, but a gradual transition between the two instability zones [Van Bragt (1998)].

Examples of mass flow rate oscillations are given in figure 2.5 for a stable (a) and an unstable case (b). It can be seen that the amplitude of the oscillations decays in the stable case and grows in the unstable case. At the stability threshold oscillations are neither decaying nor growing (not shown here).

The coupled neutronic-thermal hydraulic instabilities are also known as reactivity instabilities, because it involves the effect of a density wave on the neutronics through the density reactivity effect described in section 2.2 and illustrated in figure 2.3. Thus a power feedback mechanism is present in addition to the flow feedback described above. According to March-Leuba and Rey (1993) reactivity instabilities are far more likely to occur in BWR's than channel flow instabilities. In particular the power-transfer function described in equation 2.39 and its fuel time constant are known to have great impact on the stability of BWR's [March-Leuba and Rey (1993)]. Because of the many similarities between the two reactor types, this might as well be the case for SCWR's.

Chapter 3

Numerical Scheme

3.1 Introduction

In this chapter, the numerical scheme is described, that is used to solve the equations derived in the previous chapter. The solution algorithm and all equations, apart from those in subsection 3.4.2, were derived by Koopman (2008) for a two-phase, homogeneous equilibrium mixture flow model. Since the current work deals with supercritical flow (no phase transition) the equations from Koopman (2008) are modified, in order to only allow one-phase flow. In particular the way heat is removed from the system, differs significantly between the two-phase and the supercritical model.

3.2 Buffer vessel

The DeLight facility is kept at a constant pressure of approximately 57 bar by means of a buffer vessel positioned at the top of the loop. As the system is heating up, this buffer vessel allows for a change of volume of the set-up, to accommodate thermal expansion of the coolant. Numerically, this mechanism is treated as follows. To maintain a constant pressure, mass will be removed as the system is heating up, or added as the system is cooling down.

A mass flow rate is defined that exits or enters the system after the heat exchanger, in the horizontal section at the top of the loop in the one-dimensional system (see figure 3.2). This mass flow rate is proportional to the excess pressure:

$$M_{out} = F(p - P_{sys}) \tag{3.1}$$

Where F is a proportionality factor ($F = 6 \cdot 10^{-5}$), p the actual pressure at the node where the out- or in flow of mass occurs and P_{sys} the imposed pressure. As can be seen

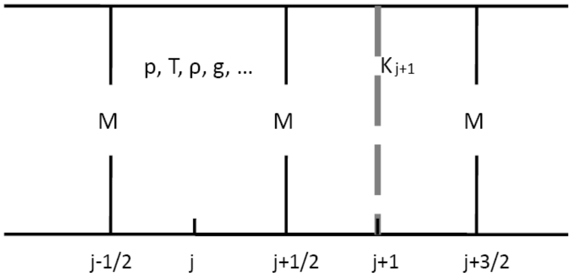

Figure 3.1: Discretization grid.

in equation 3.1, an excess pressure results in a positive value for M_{out} associated with an outflow of mass and, on the other hand, an inflow of mass will result in a negative value of M_{out}. Off course the outflow or inflow of mass will result in an outflow or inflow of energy; this is treated in section 3.4.

3.3 Discretization

For the discretization of the equations, a first order implicit up-wind scheme is chosen. An explicit method might be easier to implement, but it is also expected to require very small step sizes to avoid numerical instability. This would increase computational time drastically, where an implicit method is less prone to such instabilities and, hence, is expected to require less computational time. The up-wind scheme simulates more properly the direction of propagation of information in a flow field than a down-wind scheme does. All physical quantities are defined on a one dimensional grid. This grid and the spatial definition of the physical quantities are illustrated in figure 3.1.

As can be seen in figure 3.1, all quantities are defined inside the node of the grid except for the mass flow rate, which is defined halfway between the nodes. The complete system of equations is discretized with the use of the one dimensional grid described above.

The continuity equation (eq. 2.5) with the inclusion of mass out- and inflow described by equation 3.1 becomes:

$$A\frac{\rho_j^{n+1} - \rho_j^n}{\Delta t} = -\frac{M_{j+\frac{1}{2}}^{n+1} - M_{j-\frac{1}{2}}^{n+1} + {M_{out j}}^{n+1}}{\Delta x} \tag{3.2}$$

The subscript n denotes the number of the time step.

In order to discretize the momentum balance equation (eq. 2.19), the acceleration and friction terms are split into their current time value, depicted as $n+1$, and previous time value, n. The friction forces are by definition in the opposite direction of the flow. This characteristic is ensured by taking the absolute previous value of the flow in the frictional terms. It should be noted that the acceleration terms cannot be guaranteed to be positive, because of the impossibility of incorporating an absolute value of the current time value of the mass flow rate in the solution scheme. With the inclusion of the mass out- and inflow described by equation 3.1, the discretized momentum balance equation becomes:

$$\begin{aligned}\frac{M^{n+1}_{j+\frac{1}{2}} - M^{n}_{j+\frac{1}{2}}}{\Delta t}\Delta x + \frac{M^{n+1}_{j+1} M^{n}_{j+1}}{A\rho^{n+1}_{j+1}} - \frac{M^{n+1}_{j} M^{n}_{j}}{A\rho^{n+1}_{j}} + \frac{{M_{out}}_j^{n+1}|{M_{out}}_j^{n+1}|}{A\rho^{n+1}_{j}} = \\ A(p^{n+1}_{j+1} - p^{n+1}_{j}) - K_i\frac{M^{n+1}_{i}|M^{n}_{i}|}{2A\rho^{n+1}_{i}} - f^{n+1}_{j+\frac{1}{2}}\frac{P_w M^{n+1}_{j+\frac{1}{2}}|M^{n}_{j+\frac{1}{2}}|\Delta x}{8A^2\rho^{n+1}_{j+\frac{1}{2}}} + \rho^{n+1}_{j+\frac{1}{2}} g A \Delta x \qquad (3.3)\end{aligned}$$

Because A and Δx may vary in space, as the DeLight facility is not of uniform cross-sectional area and the one-dimensional spatial grid is not equidistant, there should have been definitive spatial indices on A and Δx. However, for better legibility these are left out. The mass flow rates in the acceleration terms are subscripted with indices inside a node of the grid, although they are not defined there. (See figure 3.1) At these places where the mass flow rate is undefined the best estimate is given by the nearest value of the mass flow rate counter-directional to the flow, i.e. its upwind neighbour. For this reason the indices in question are subject to flow reversals. The index j becomes $j - \frac{1}{2}$ if the flow is in the positive x-direction or $j + \frac{1}{2}$ if the flow is in the negative x-direction. From this point on this upwind scheme should be assumed whenever quantities are subscripted with an index of a position where the quantity is not defined.

Again with the inclusion of mass in- and outflow the enthalpy balance equation is discretized. The enthalpy of the entering or exiting flow h_{out} will be defined in section 3.4.

$$\begin{aligned}A\frac{\rho^{n+1}_{j} h^{n+1}_{j} - \rho^{n}_{j} h^{n}_{j}}{\Delta t} + \frac{M^{n+1}_{j+\frac{1}{2}} h^{n+1}_{j+\frac{1}{2}} - M^{n+1}_{j-\frac{1}{2}} h^{n+1}_{j-\frac{1}{2}}}{\Delta x} + \frac{{M_{out}}_j^{n+1}{h_{out}}_j^{n+1}}{\Delta x} \\ = {q'}^{n+1}_{j} + A\frac{p^{n+1}_{j} - p^{n}_{j}}{\Delta t} \qquad (3.4)\end{aligned}$$

At last equation 2.14 is discretized:

$$\rho^{n+1}_{j} = \rho^{n}_{j} + \frac{\partial \rho^{n}_{j}}{\partial T^{n}_{j}}(T^{n+1}_{j} - T^{n}_{j}) + \frac{\partial \rho^{n}_{j}}{\partial p^{n}_{j}}(p^{n+1}_{j} - p^{n}_{j}) \qquad (3.5)$$

3.4 Algorithm

Because the equations governing the flow are inter-dependent, some attention must be paid to the solution scheme in order to solve the entire system. A specific algorithm is iterated until a convergence criterion is reached. In this section the details of this algorithm will be discussed.

The enthalpy is determined directly from the enthalpy balance equation. However, equation 3.4 cannot be calculated, because the density, mass flow rate and pressure of the next time- or iteration-step are still unknown. By deducting the discretized continuity equation (eq. 3.2) from the discretized enthalpy balance equation (eq. 3.4) the unknown density is taken out of the equation:

$$\underbrace{Ah_j^{n+1}\frac{\rho_j^{n+1}-\rho_j^n}{\Delta t} + h_j^{n+1}\frac{M_{j+\frac{1}{2}}^{n+1} - M_{j-\frac{1}{2}}^{n+1} + {M_{out}}_j^{n+1}}{\Delta x}}_{=0} +$$
$$A\rho_j^n\frac{h_j^{n+1}-h_j^n}{\Delta t} + \frac{M_{j-\frac{1}{2}(j+\frac{1}{2})}^{n+1}h_{j(j+1)}^{n+1} - M_{j-\frac{1}{2}(j+\frac{1}{2})}^{n+1}h_{j-1(j)}^{n+1}}{\Delta x} +$$
$$\frac{{M_{out}}_j^{n+1}({h_{out}}_j^{n+1} - h_j^{n+1})}{\Delta x} = {q'}_j^{n+1} + A\frac{p_j^{n+1}-p_j^n}{\Delta t} \tag{3.6}$$

Where the double subscripts in the fourth left hand term refer to forward or backward (in brackets) flow. From this point on forward flow will be assumed and the double index will be omitted. Although the unknown value of the density is no longer present in the equation, the unknown values of mass flow rate and pressure still are. To overcome this problem the algorithm is iterated in order to converge to a general solution of all balance equations in terms of quantities that closely resemble the true solution at that particular time-step. This results in a discretized enthalpy balance equation with the superscript k denoting the iteration value:

$$A\rho_j^n\frac{h_j^{k+1}-h_j^n}{\Delta t} + \frac{M_{j-\frac{1}{2}}^k h_j^{k+1} - M_{j-\frac{1}{2}}^k h_{j-1}^{k+1}}{\Delta x} +$$
$$\frac{{M_{out}}_j^k({h_{out}}_j^{k+1} - h_j^{n+1})}{\Delta x} = {q'}_j^{n+1} + A\frac{p_j^{n+1}-p_j^n}{\Delta t} \tag{3.7}$$

The enthalpy associated with the mass outflow (in the horizontal section after the heat exchanger) is defined equal to the enthalpy in the node that allows the outflow: $h_{out} \equiv h$. With this definition it is easy to see that the mass outflow in the third left hand term of equation 3.7 is dropped entirely out of the enthalpy balance equation. Because the heat flux from the coolant in the heat exchanger defined in equation

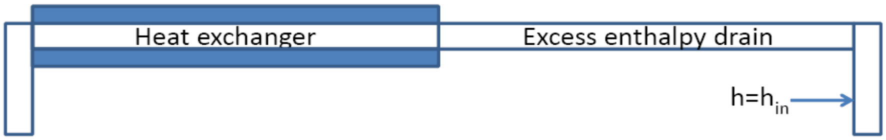

Figure 3.2: Schematic drawing of the top of the one dimensional loop, in order to depict the position of the heat exchanger, the enthalpy drain and the nodes where the enthalpy is set to the desired inlet enthalpy.

2.12 does not necessarily guarantee removal of all heat added to a volume of coolant travelling through the loop, the core inlet enthalpy is not necessarily constant either. This resulted in difficulties when convergence tests were performed, while developing the code. Therefore a specific section of the system forces the desired inlet enthalpy h_{in} upon the coolant at the exit of the heat exchanger. This section is depicted in figure 3.2. The excess (or deficit of) enthalpy in a node amounts to $(h_j - h_{in})\rho_j A\Delta x$. In the horizontal section after the heat exchanger, the enthalpy in excess of the desired inlet enthalpy is drained. In the case of a lack of enthalpy extra energy is added. A 'relaxation constraint', λ_j is added to avoid large gradients in the system. It is a function that gradually goes to one in the first few nodes after the heat exchanger and is one for the remaining horizontal part up to the downcomer (elsewhere it is zero). After this section the enthalpy is very close but not necessarily equal to the desired inlet enthalpy. This leads to the final form of the one-dimensional enthalpy balance equation:

$$\begin{aligned} &A\rho_j^n \frac{h_j^{k+1} - h_j^n}{\Delta t} + \frac{M^k_{j-\frac{1}{2}} h_j^{k+1} - M^k_{j-\frac{1}{2}} h_{j-1}^{k+1}}{\Delta x} \\ &= {q'}_j^{n+1} + A\frac{p_j^{n+1} - p_j^n}{\Delta t} - \lambda_j A\rho_j \frac{(h_j^{k+1} - h_{in})}{\Delta t} \end{aligned} \tag{3.8}$$

In the first ten nodes of the downcomer, where the enthalpy now is close to the desired inlet enthalpy, the enthalpy is set equal to the desired inlet enthalpy. This last step finally results in a constant enthalpy, that can be set to a specific value, at the inlet of the core section.

The next step in the algorithm is the determination of the temperature. Experience from Koopman (2008) showed that it was beneficial for the numerical stability of the code to reference the thermodynamic properties package NIST [Huber et al. (2002)] to provide the temperature at the new iteration value from known values of enthalpy and pressure. Equation 3.5 is used to calculate the density.

$$\rho_j^{k+1} = \rho_j^k + \frac{\partial \rho_j^k}{\partial T_j^k}(T_j^{k+1} - T_j^k) + \frac{\partial \rho_j^k}{\partial p_j^k}(p_j^k - p_j^{k-1}) \tag{3.9}$$

The NIST [Huber et al. (2002)] properties package is also referenced to provide the partial derivatives of the density with respect to the temperature, respectively pressure, given the temperature and density. It should be noted that the iteration values of p are one less than those of T, because the pressure has not yet been determined.

3.4.1 Pressure correction

Apart from the unknown pressure, the momentum balance equation can be calculated implicitly. So first the determination of pressure will be discussed in this section. The pressure correction method developed by Wesseling et al. (1995) and extended to compressible flow by Bijl (1999) is used to adjust the pressure in such a way that it corrects the mass flow rate in order to preserve mass. This is done by analyzing the difference in mass flow rate as it is calculated with an implicit and an explicit pressure. If the mass flow rate correction, M', is defined as:

$$M' = M^{k+1}(p^{k+1}) - M^*(p^k) \tag{3.10}$$

in which M^* is a prediction for the mass flow rate based on the previous iteration value of the pressure and for every iteration a new prediction is made. The subtraction of the two momentum balance equations, neglecting the friction and acceleration terms, and substituting $p' = p^{k+1} - p^k$ leads to:

$$\frac{M'_{j+\frac{1}{2}}}{\Delta t} = -A\frac{p'_{j+1} - p'_j}{\Delta x} \tag{3.11}$$

Then, the equation of state (eq. 3.9) is employed into the continuity equation (eq. 3.2) to account for the change in density:

$$\frac{A}{\Delta t}\frac{\partial \rho_j^k}{\partial T_j^k}(T_j^{k+1} - T_j^k) + \frac{A}{\Delta t}\frac{\partial \rho_j^k}{\partial p_j^k}(p_j^{k+1} - p_j^k) = -\frac{M_{j+\frac{1}{2}}^{k+1} - M_{j-\frac{1}{2}}^{k+1} + {M_{out}}_j^{k+1}}{\Delta x} \tag{3.12}$$

Now M^{k+1} and p^{k+1} are replaced by $M' + M^*$ and $p' + p^k$ respectively and substituting equation 3.1 in equation 3.12 leads to the final expression for the pressure correction:

$$A\frac{\Delta t}{\Delta x}(p'_j - p'_{j-1}) - A\frac{\Delta t}{\Delta x}(p'_{j+1} - p'_j) + Fp'_j + A\frac{\Delta x}{\Delta t}\frac{\partial \rho_j^k}{\partial p_j^k}p'_j = M^*_{j-\frac{1}{2}} - M^*_{j+\frac{1}{2}} - F(p_j^k - P_{sys}) - A\frac{\Delta x}{\Delta t}\frac{\partial\rho_j^k}{\partial T_j^k}(T_j^{k+1} - T_j^k) \tag{3.13}$$

The pressure correction can be calculated from this equation and by combining it with equation 3.1 the mass outflow M_{out} can be obtained, as well as the mass flow rate correction M' with equation 3.11. The discretized momentum balance equation for the pressure correction scheme is then written in terms of the predicted mass flow rate M^*:

$$\frac{M^*_{j+\frac{1}{2}} - M^k_{j+\frac{1}{2}}}{\Delta t}\Delta x + \frac{M^*_{j+1}M^k_{j+1}}{A\rho^{k+1}_{j+1}} - \frac{M^*_j M^k_j}{A\rho^{k+1}_j} + \frac{{M_{out}}_j^k|{M_{out}}_j^k|}{A\rho_j^{k+1}} = A(p^k_{j+1}-p^k_j) - K_i\frac{M_i^*|M_i^k|}{2A\rho_i^{k+1}} - f^{k+1}_{j+\frac{1}{2}}\frac{P_w M^*_{j+\frac{1}{2}}|M^k_{j+\frac{1}{2}}|\Delta x}{8A^2\rho^{k+1}_{j+\frac{1}{2}}} + \rho^{k+1}_{j+\frac{1}{2}}gA\Delta x \tag{3.14}$$

3.4.2 Neutronic feedback implementation

The program starts with the coolant at a constant temperature throughout the loop and initially at rest. At this moment no heat is added or extracted from the system. The linear heat rate, q', in the core sections and in the heat exchanger gradually rises to the desired level at a specified rate during the warm-up period. After this warm-up period, the program is run long enough for a steady state solution to be reached. When a steady state solution has been reached, the program calculates the average coolant density in the core.

At steady state the change in neutron density and the change in precursor concentrations must be zero. The next time step, a neutronic feedback mechanism is turned on. To keep track of the relative perturbation of the neutron density, equations 2.35 and 2.36 are discretized. With the subscript n depicting the number of the time step Δt:

$$\underline{n}'^{n+1}\left(\frac{1}{\Delta t} - \frac{\rho^{n+1}_{reactivity} - \beta}{\Lambda_{gen}} - \sum_{i=1}^{6}\frac{\lambda_i}{1/\Delta t + \lambda_i}\frac{\beta_i}{\Lambda_{gen}}\right) = \frac{\rho^{n+1}_{reactivity}}{\Lambda_{gen}} + \frac{1}{\Delta t}\underline{n}'^{n} + \sum_{i=1}^{6}\frac{\lambda_i}{1+\lambda_i\Delta t}\underline{C}_i'^{n} \tag{3.15}$$

$$\underline{C}_i'^{n+1}\left(\frac{1}{\Delta t} + \lambda_i\right) = \frac{\beta_i}{\Lambda_{gen}}\underline{n}'^{n+1} + \frac{1}{\Delta t}\underline{C}_i'^{n}, \quad i = 1, ..., 6 \tag{3.16}$$

Combining the relative perturbation of the neutron density with equation 2.34 and the power at steady state, results in a value for the perturbation of the power, p'. As was stated in chapter 2 the change in linear heat rate, q'_{extra}, in the reactor core is not instantaneous with the change in power. The power-transfer function (given by equation 2.39) that relates q'_{extra} at the n^{th} time step to the change in power, p', at the n^{th} time step is

$$G_F(z) = \frac{\underline{q}'_{extra}(z)}{\underline{p}'(z)} \tag{3.17}$$

Rearranging equation 2.39 and equation 3.17 gives

$$\underline{q}'_{extra}(z) = \left[\frac{1}{b_1 + b_2 z^{-1}}\right] \underline{p}'(z) \tag{3.18}$$

$$\underline{q}'_{extra}(z) = \frac{1}{b_1}\left(\underline{p}'(z) - b_2 \underline{q}'_{extra}(z) z^{-1}\right) \tag{3.19}$$

Taking the inverse z-transform:

$$\underline{q}'^{n}_{extra} = \frac{1}{b_1}\left(\underline{p}'^{n} - b_2 \underline{q}'^{n-1}_{extra}\right) \tag{3.20}$$

Therefore, with equation 3.20, the change in linear heat rate in the core as a result of the neutronic coolant density feedback mechanism is known. In order to simplify implementation and computation of the transfer function, the order of execution of the transfer function and calculation of the linear heat rate is altered. The transfer function is carried out on the relative neutron density perturbation and results in an effective relative neutron density perturbation $\underline{N}'$, from which the effective linear heat rate can be calculated [Rohde (2010)]. Because the linear heating rate is directly proportional to the effective neutron density:

$$\underline{N}' = \underline{q}'_{extra} \tag{3.21}$$

Substituting equations 2.34 and 3.21 in equation 3.20:

$$\underline{N}'^{n} = \frac{1}{b_1}\left(\underline{n}'^{n} - b_2 \underline{N}'^{n-1}\right) \tag{3.22}$$

At a specific time, the steady state solution is perturbed by a small increase in linear heat rate (default value is 1%) during one time step. Apart from this single perturbation, the program runs in the same manner as described in subsection 3.4.4. The dynamic behaviour of the mass flow rate at the core inlet resulting from the perturbation, is analyzed to gain insight into the stability of the system.

3.4.3 Solving the system of equations

The total number of nodes is defined as N, so every discretized balance equation forms a linear system of equations with size N. Each system of equations can be written in matrix form as:

$$\underline{\underline{A}}\,\underline{\phi} = \underline{s} \tag{3.23}$$

Where $\underline{\phi}$ is a vector carrying the next value $k+1$ of the variable that is to be calculated. This can be h, M^* or p'. All the terms of the equation that are independent of $\underline{\phi}$ are gathered in the solution vector $\underline{s}$, $\underline{\underline{A}}$ is a cyclic tri-diagonal matrix carrying all the terms dependent on $\underline{\phi}$. The code describes a closed loop, hence the first node depends on the last one and vice-versa. Because of this, $\underline{\underline{A}}$ is cyclic. Also due to the upwind scheme each node can be dependent on either neighbour, therefore $\underline{\underline{A}}$ is tri-diagonal as well. This system of equations can be solved with the Sherman-Morrison method for cyclic tri-diagonal matrices. Below it will be briefly summarized. A more elaborate description of this method can be found in Koopman (2008) or in Press et al. (1992).

The Sherman-Morrison method describes $\underline{\underline{A}}$ as an ordinary non-cyclic tri-diagonal matrix $\underline{\underline{A'}}$ with a perturbation $\underline{u} \otimes \underline{v}$ such that:

$$\underline{\underline{A}}\,\underline{\phi} = (\underline{\underline{A'}} + \underline{u} \otimes \underline{v})\underline{\phi} = \underline{s} \tag{3.24}$$

When $\underline{\underline{A}}$ is defined as

$$\underline{\underline{A}} = \begin{bmatrix} a_1 & c_1 & \dots & & \beta \\ b_2 & a_2 & \dots & & \\ & & \dots & & \\ & & \dots & a_{N-1} & c_{N-1} \\ \alpha & & \dots & b_N & a_N \end{bmatrix}, \tag{3.25}$$

$\underline{\underline{A'}}$, $\underline{u}$ and $\underline{v}$ are defined as

$$\underline{\underline{A'}} = \begin{bmatrix} a_1-\gamma & c_1 & \dots & & 0 \\ b_2 & a_2 & \dots & & \\ & & \dots & & \\ & & \dots & a_{N-1} & c_{N-1} \\ 0 & & \dots & b_N & a_N - \frac{\alpha\beta}{\gamma} \end{bmatrix}, \underline{u} = \begin{bmatrix} \gamma \\ 0 \\ \vdots \\ 0 \\ \alpha \end{bmatrix} \text{ and } \underline{v} = \begin{bmatrix} 1 \\ 0 \\ \vdots \\ 0 \\ \frac{\beta}{\gamma} \end{bmatrix} \tag{3.26}$$

With γ an independent parameter that can be set to any value. If for the vectors $\underline{y}$ and $\underline{z}$ the following holds:

$$\underline{\underline{A'}}\,\underline{y} = \underline{s} \tag{3.27}$$

and

$$\underline{\underline{A'}}\,\underline{z} = \underline{u} \tag{3.28}$$

Then the solution to the system (eq. 3.23) is given by

$$\underline{\phi} = \underline{y} - \left[\frac{\underline{v}\cdot\underline{y}}{1+\underline{v}\cdot\underline{z}}\right]\underline{z} \tag{3.29}$$

The non-cyclic tri-diagonal systems of equations 3.27 and 3.28 can be solved with an algorithm described by Holmes (1999).

3.4.4 Overview of the solution algorithm

As was pointed out earlier the algorithm described above will be iterated until convergence is reached. The convergence criterion is satisfied when the new iterated value for the pressure p^{k+1} is within a specified limit (0.1%) of the previous iteration value p^k, everywhere in the system. An overview of the solution algorithm follows below:

1. Find the physical quantities ρ, $\frac{\partial\rho}{\partial T}$ and $\frac{\partial\rho}{\partial p}$.
2. Use equation 3.7 (and possibly equation 3.20) to compute h^{k+1}.
3. Find the temperature T^{k+1} from NIST with h^{k+1} and p^k.
4. Compute ρ^{k+1} using equation 3.9.
5. Compute M^* using equation 3.14.
6. Use equation 3.13 to find p^{k+1} and with equations 3.1 and 3.10 find M^{out} and M^{k+1} respectively.
7. Iterate steps 1 to 6 until the convergence criterion is satisfied.
8. Store each variable to the new time value.

Chapter 4

Experimental facility

4.1 Downscaling the HPLWR

The stability of a natural circulation driven HPLWR can be studied by means of a scaled down test facility. A scaling fluid is used to alleviate the pressure- and temperature level and the power requirements, in order to operate at more suitable lab conditions. The equations that govern the flow in the HPLWR need to be considered and made non-dimensional so a scaled test facility can be designed, where the physics involved is the same as in the original unscaled system. The scaling procedure is described by Rohde et al. (2011) and for the selected scaling fluid, Freon R23, a number of scaling factors are derived. Some of these scaling factors can be found in appendix B. As a result of the scaling procedure the nominal operating pressure is reduced from 250 bar to 57 bar. The nominal core inlet and outlet temperature become -21 ^{0}C and 105 ^{0}C instead of 280 ^{0}C and 500 ^{0}C and the nominal power is reduced to 9 kW. The experimental work described in this chapter was carried out by T'Joen et al. (2011). A description of the experimental set-up and procedure is given below.

4.2 DeLight facility

At the Delft University of Technology an experimental facility, named DeLight, is constructed according to the scaling rules. The geometry of the facility is schematically depicted in figure 4.1. The height of the loop is 10 m and it consists of stainless steel tubing with an internal diameter of 6 mm for the core sections and 10 mm for the riser and downcomer. The maximum power of the facility is 18 kW, which is divided over four heated tube sections (three core sections and a moderator channel in the downcomer, mimicking the HPLWR water rods). Heating is done electrically by sending a current through the tubes. This provides a uniform heat flux over each individual heated

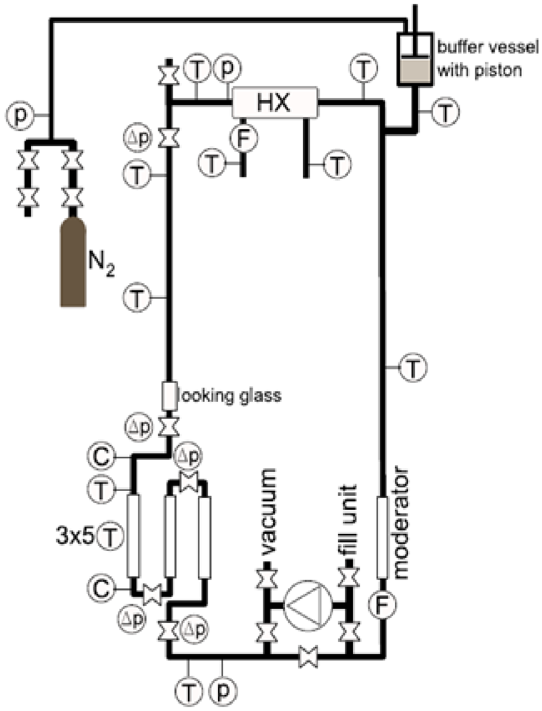

Figure 4.1: A schematic representation of the DeLight facility [Figure from T'Joen et al. (2011)].

section. The power distribution in the three-pass HPLWR core is non uniform. [Fisher et al. (2009)] Therefore the power rating of each heated section of the facility can be controlled separately, so a non-uniform power distribution can be applied over the three different core sections. During experiments the standard distribution of power will be: 53% over the first-, 30% over the second- and 17% over the third core section. PEEK rings mounted in between two flanges ensure electrical insulation of each core from the rest of the system. Valves are installed between the core sections, at the in- and outlet of the core and at the top of the riser. These can be used to introduce local friction values in the system, for example to mimick the mixing plena from the three-pass core design.

The pressure level of the facility is controlled with a buffer vessel at the top of the loop. In the vessel a piston is connected to a nitrogen gas cylinder. By adjusting the position of this piston the pressure can be set to the desired value. To remove heat from the system, two heat exchangers are installed in series at the top of the loop. These heat exchangers provide control over the core inlet conditions as well. The first heat exchanger uses cooling water to reduce the temperature of the coolant to $17\,^0$C. The second one is an evaporator with R507a, that further reduces the coolant temperature to a minimum of -25 ^{0}C. This temperature can be controlled by adjusting the saturation pressure on the secondary side.

Since the three core sections will have a large difference in temperature profile, the set-up must allow for thermal expansion of the different core sections. Therefore, the connection of the core sections to the wall and bottom has to be non-rigid. The tubes are connected to the wall using moveable spacers that contain pre-stressed springs. As such, the thermal expansion differences are in part compensated by the stress on the springs. The bottom connection between the different core sections is made from a flexible tube of woven steel.

Measurements on the facility are done with the help of a large number of sensors. Absolute pressure sensors (denoted by a p-symbol in figure 4.1) are present at the top and bottom of the loop. Furthermore, each valve in the system is combined with a differential pressure drop sensor (Δp-symbol in figure 4.1) to measure the local pressure drop. To measure the local fluid temperature, five type K thermocouples are located in each core section. These thermocouples are also electrically insulated with PEEK rings to prevent the feed current from passing through. The individual thermocouple channels were calibrated using three reference thermocouples, that were calibrated over the entire temperature range by a certified body. In the riser, the downcomer and on the secondary side of the heat exchangers additional thermocouples are installed as can be seen in figure 4.1. The mass flow rate is measured using a Coriolis meter (denoted by a F-symbol in figure 4.1). To reduce the exchange of heat with the environment the tubing of the system is insulated using a layer of 25 mm of Armacell$^©$. Although a magnetic rotor pump is present in the system, a bypass can be used to allow for natural circulation.

Monitoring of the experimental set-up and recording of the sensor signals is done with a PC with a National Instruments (NI) PCI-6259 data acquisition card, connected to a NI SCXI-1001 rack with two SCXI-1102B 32-channel amplifiers. With this set-up, up to 64 multiplexed signals are recorded for further analysis. A separate data acquisition system with a NI-6035 DAQ card is used for safety monitoring. It shuts down the power supplies if one of either three temperature values, two pressure values, the R23 flow rate or the heat exchanger cooling water flow rate exceeds prescribed limits.

To implement the feedback effect of coolant density perturbations on the reactivity, the average core density is measured with the help of the 15 thermocouples installed in the core sections and the equation of state for the density. The values are measured over a period long enough to determine the average steady state value of the density in the core. When the neutronic feedback is activated, the reactivity and the resulting change in power are calculated as described in section 2.2 and 3.4.2 with the help of a linearized six-group, point-kinetic model for the neutron density. To account for the delay by the transfer of heat through a fuel rod, the same first order transfer function is used as was described in section 3.4.2.

4.3 Experimental procedure

The stability of the experimental set-up is determined with the following procedure. The circulation of the R23 in the loop is started with help of the pump and 1 kW of heating is added. Then the pump is switched off and bypassed, resulting in natural circulation of the fluid. Next, the pressure is raised above the supercritical pressure and the heat exchangers are turned on. The system is then brought to the desired testing conditions, by simultaneously incrementing the power in the core sections and controlling the position of the piston in the buffer vessel. The system is said to be in a steady state if the absolute pressure variations are roughly 0.25 bar and temperature oscillations are below 0.2 K, for a specific pressure with a specified power distribution over the core sections. When the set-up reaches a steady state the measurement is started. First the average coolant density in the core is measured during two minutes. These values are averaged to obtain the steady state average coolant density. Then the neutronic feedback mechanism is turned on, with a power correction calculated with the difference between the measured average coolant density and the steady state value.

If the case that is being studied is unstable, the power input will fluctuate with a growing amplitude as a result of the neutronic feedback mechanism. The signals of the set-up are then recorded until a certain power saturation is reached. This saturation value is set to 10% of the original power input to prevent large pressure fluctuations in the loop. When no oscillations are present two minutes after the neutronic feedback mechanism is turned on, the system is found to be stable. After these two minutes the power is increased with a step of 250 or 500 W during five seconds. The resulting decaying signals are then recorded until they are no longer distinguishable. The oscillations were most obvious in the temperature signal at the inlet of the riser during experiments.

Signal analysis tools are used to process the recorded signals. All sensor signals are sampled with a frequency of 120 Hz and resampled to 20 Hz. Before resampling the signals are filtered with a cut-off frequency of 9 Hz with a digital filter in Matlab. This is done to prevent aliasing, which can occur according to the Nyquist theorem when a signal is down-sampled without low-pass filtering.[Oppenheim and Willsky (1997)] The resampling is performed by averaging each six samples. The resampled data is then used to determine the decay ratio (DR).

The equation $y = (1 - c - a)\cdot e^{b_1 t} + c + a\cdot e^{b_2 t}\cdot cos(\omega t)$ is fitted to the first two periods of the auto-correlation function of the signal. The decay ratio is then defined by:

$$DR = e^{2\pi b_2/|\omega|} \tag{4.1}$$

These equations are derived by Marcel (2007) for a natural circulation BWR. Standard error analysis procedures can be used to determine the uncertainty in the decay ratio and it was found to be less than 5%. The auto power spectral density is also determined and the presence of a single well-defined peak at the resonance frequency ω, is verified as an extra check for that resonance frequency.

Chapter 5

Results

5.1 Benchmarking

5.1.1 Comparison of power-flow map with literature

To evaluate the performance of the solution algorithm for steady state flow rates, the code is benchmarked with a code found in literature. Our own code is used to determine a power-flow map for a supercritical CO_2 loop as described by Jain and Rizwan-uddin (2008). A schematic representation of this loop is given in figure 5.1(a). The system consists of four straight tube sections with an inner diameter of 0.07484 m, so the flow area is constant throughout the loop. The vertical sections are 10 m long and they are connected at the top and bottom by horizontal sections of 6 m length. Heating takes place over a length of 2 m, at the center of the bottom section. Cooling takes place over a length of 1 m, at the center of the top section. The heat source and sink are of equal magnitude and both uniformly distributed along the respective sections. Furthermore, energy is directly deposited to or extracted from the system. At the bottom-corner of the loop, before the core inlet, a boundary condition is imposed by means of a buffer vessel ($T = 25\,^0\mathrm{C}$, $p = 8\,\mathrm{MPa}$) with a flow orifice at the in- and outlet of the vessel: $K_{in} = K_{out} = 1$.

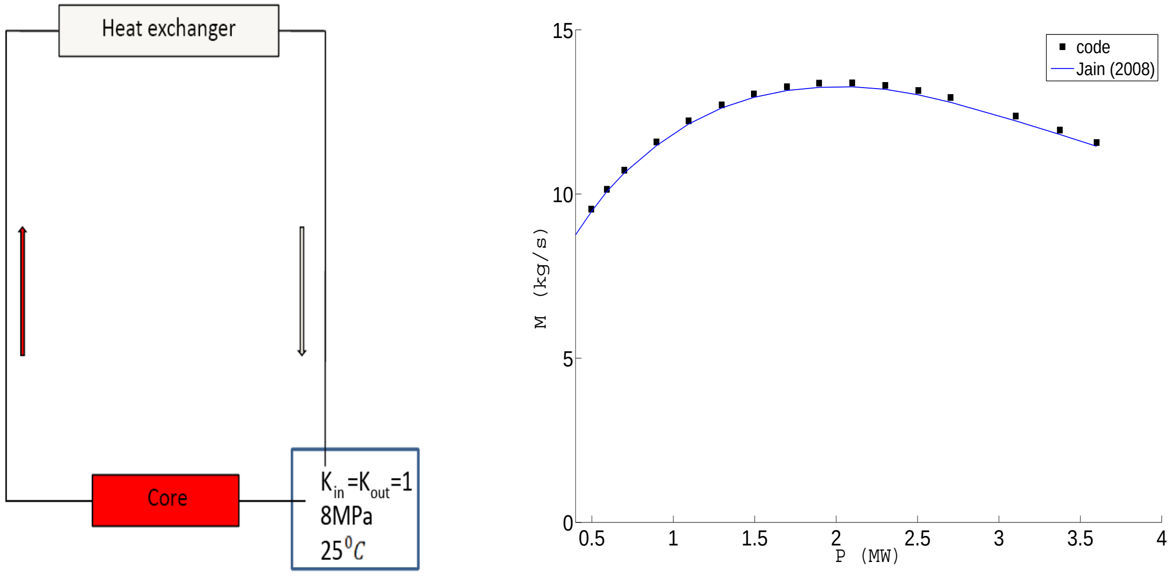

(a) (b)

Figure 5.1: Schematic representation of the supercritical CO_2 loop described by Jain and Rizwan-uddin (2008) and comparison of power-flow maps. Results are generated with Δx=0.2 cm and Δt=0.35 s using the own code.

A comparison of power-flow maps produced with the code described by Jain and Rizwan-uddin (2008) and the own code is given in figure 5.1(b). Very good agreement is found between the two power flow maps (deviations are between 0.6 and 1.2% of the results of Jain and Rizwan-uddin (2008)).

It should be pointed out that the description of the flow orifices in Jain and Rizwan-uddin (2008) is rather vague. A value of $K_{in} = K_{out} = 0.5$ is stated, but this resulted in an over prediction of the mass flow rate by the own code of 6-8% of the results of Jain and Rizwan-uddin (2008). Another code (by T'Joen) also predicted higher steady state mass flow rates. However, with $K_{in} = K_{out} = 1$, very good agreement was found with the results by Jain and Rizwan-uddin (2008) for both codes.

5.1.2 Power-flow map of the DeLight facility

Before a comparison of the power-flow maps generated by the code and measured in the DeLight facility can be presented, it is important to point out a difference between the geometry of the facility and the geometry described by the code. For ease of implementation and to reduce computational time, the two heat exchangers present in the DeLight facility are modelled as one simple system. In the code both heat exchangers are represented by a straight, horizontal tube from the top of the riser to the top of the downcomer, with a constant diameter equal to that of the riser and downcomer. In reality however, the complicated interior geometry of the heat exchangers results in an unknown, most likely larger friction. By modelling the heat exchangers as a straight tube, it is expected that the total friction in the loop will be underestimated, resulting in predictions of mass flow rate for the system that are too low compared to the measured values. Therefore, a multiplication factor, $fr_{HX} = 8.86$, is introduced which is multiplied with the calculated friction in the heat exchanger tube given by equation 2.16 (Haaland correlation):

$$f = fr_{HX} \cdot f(Re) \tag{5.1}$$

This value was determined by matching the code results to experimental data for one specific case ($P = 8.014\,\mathrm{kW}$, $p = 57.6\,\mathrm{bar}$, $T_{in} = -3.9\,^0\mathrm{C}$). A power-flow map was determined and compared to experiments in the DeLight facility with the same power distribution, system pressure and inlet temperature. It should be noted explicitly that these variables varied over different experiments. The results, generated with a grid size of 0.5 cm and a time step of 0.1 s, are shown in figure 5.2.

It can be seen that for powers between 3 and 8 kW the steady state mass flow rate as predicted by the code is within 4% of the experimental value. For lower power, deviations can be larger. At this moment no experimental steady state data is available for higher powers, so it is impossible to verify the accuracy of the mass flow rate predictions by the code for powers above 8 kW.

During simulations it was found that the steady state mass flow rate did depend on the pre-set length of the warm-up period. This was most obvious for powers above 5 kW, where a short warm-up period resulted in large deviations of the mass flow rate compared to the experiments. Extending the warm-up period resulted in converging solutions for the steady state mass flow rate that closely resemble the experiments. Special care was taken to select a warm-up period long enough to obtain an accurate steady state mass flow rate prediction. Furthermore, the mechanism leading to the different steady state mass flow rate predictions is studied extensively to gain insight into this phenomenon.

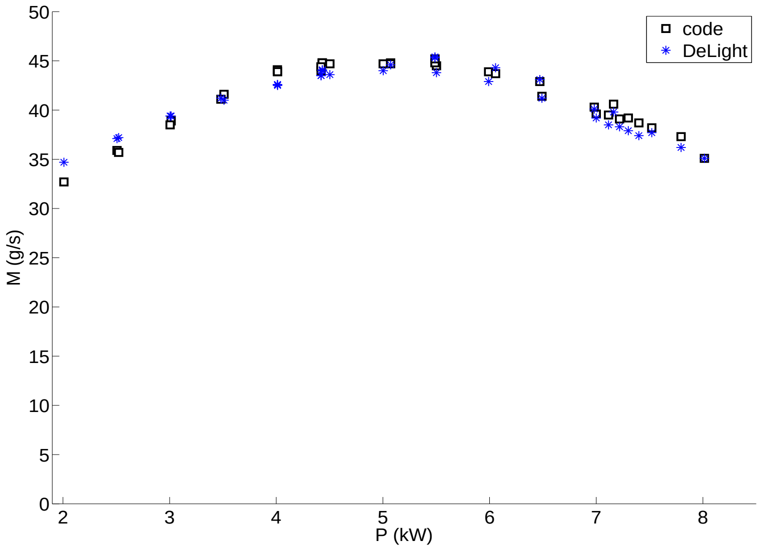

Figure 5.2: Power-flow maps from the DeLight facility and the code generated with $\Delta x = 0.5cm$ and $\Delta t = 0.1s$ to validate the friction multiplication factor in the modelled heat exchanger.

5.1.3 Obtaining the correct steady state conditions

In order to study the dynamic behaviour of the system, it is of great importance to accurately predict the steady state. Simulations with relatively high power showed that the length of the warm-up period does influence the steady state solution for the mass flow rate. Since the existence of multiple steady state solutions (for a given power, pressure and inlet temperature) is impossible, a thorough analysis is done of the simulations leading to the different steady state solutions. It was found that different steady state mass flow rate predictions only seem to occur for powers above 5 kW (with $T_{in} = 0\,^0$C). As can be seen in figure 5.2 this corresponds approximately to the top of the power-flow curve.

After analysis of the temporal behaviour of the mass flow rate during the warm-up period, it was found that the different steady state mass flow rate predictions are the result of growing oscillations of the mass flow rate. These oscillations occur in the simulations at higher power, but can suddenly start to decay rapidly with another frequency, after reaching large amplitudes. These irregularly decaying oscillations lead to an incorrect steady state prediction. The mass flow rate at the core inlet of a simulation where these oscillations occur is depicted in figure 5.3.

The oscillations occur when the power is increased too rapidly above the power belonging to the top of the power-flow curve. By carefully selecting an appropriate warm-up rate it is possible to eliminate these erratic oscillations and an accurate steady state

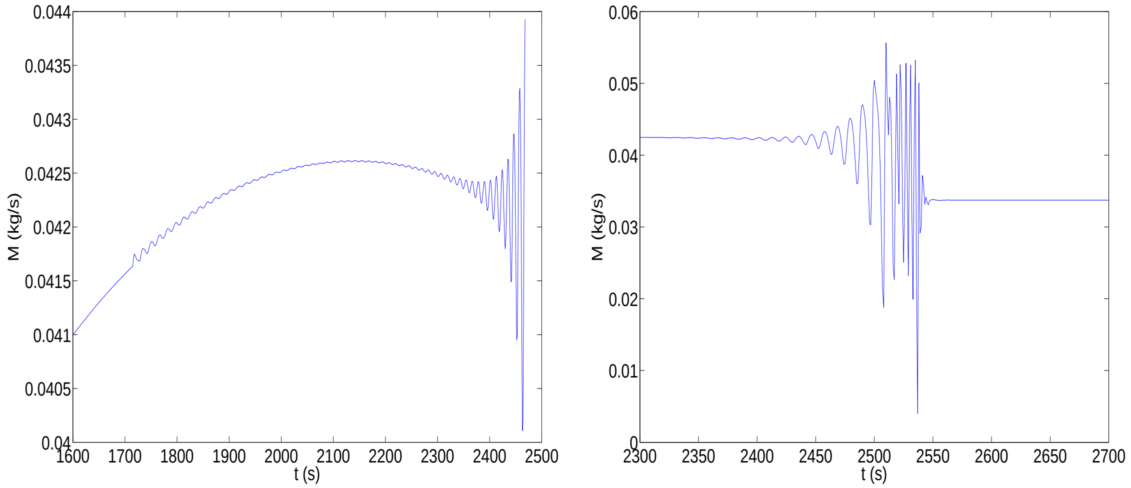

(a) *(b)*

Figure 5.3: Growing oscillations of the mass flow rate at the core inlet (a) and erratic decay of the oscillations with a different frequency (b) leading to an inaccurate steady state solution for $P = 5.7\,kW$*,* $T_{in} = 0\,^0C$*,* $\Delta x = 0.1cm$ *and* $\Delta t = 25ms$ *at 57 bar.*

mass flow rate prediction can be obtained. Dynamic mass flow rate data generated by the code must therefore always be checked for the presence of these oscillations, since only steady state solutions reached without these oscillations are suitable for analysis of the stability of the system.

Experience during simulations has shown that a more gradual increase in power reduces the occurrence of these oscillations. But since a slow warm-up rate results in a long warm-up period in order to achieve high power, the computational time needed to obtain a steady state can become very long. An effective method to reduce the time needed to obtain a steady state solution, is to increase the power rapidly in the beginning- and slow at the end of the warm-up period. This can be done for example by describing the time dependent power $P(t)$, during the warm-up period as:

$$P(t) = P_{steady}\left\{1 - exp(-c_1 t)\right\} \tag{5.2}$$

With P_{steady} the desired steady state power. The constant c_1 determines the magnitude of the increase in power during the warm-up period. Figure 5.4 shows the development of a steady state solution for $P = 5.7\,\text{kW}$ and $T_{in} = 0\,^0\text{C}$ at 57 bar with equation 5.2, ($c_1 = 1/300$) during a warm-up period of 2000 s.

A power-flow curve for $T_{in} = 0\,^0\text{C}$ at 57 bar is shown in figure 5.5. The steady state data generated with the use of equation 5.2 ($c_1 = 1/300$, during a warm-up period of 2000 s) results in a smooth curve. The data generated with a linear increase in power (during a warm-up period of 2500 s) displays a ‘kink’ after the maximum of the power flow curve, where the oscillations described earlier were present.

The mass flow rate oscillations that occur if the power is increased too rapidly, were

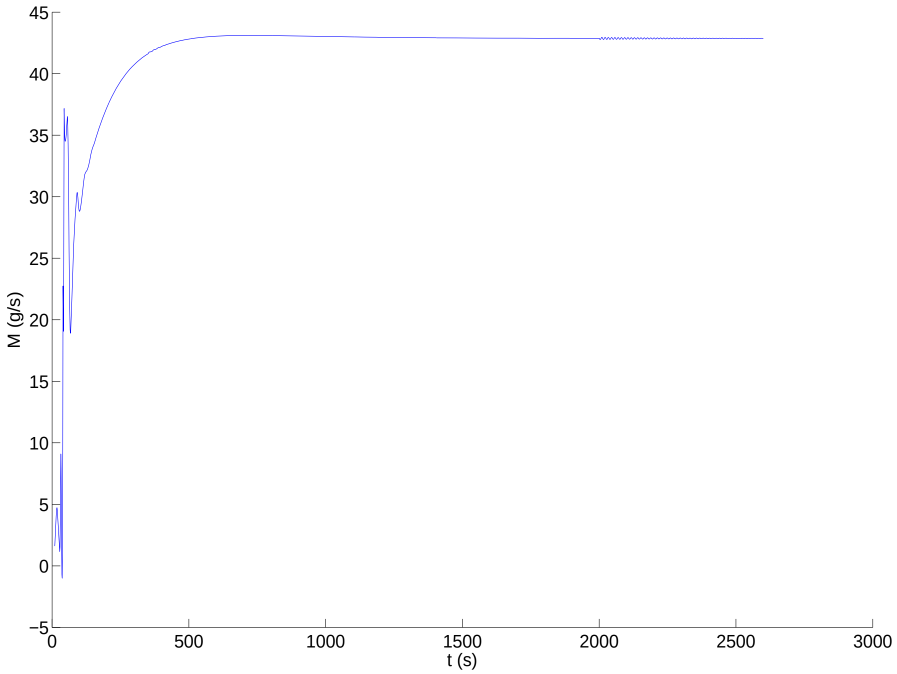

Figure 5.4: Warm-up period of 2000 s to reach steady state solution for $P = 5.7\,kW$ *and* $T_{in} = 0\,^0C$ *at 57 bar with equation 5.2. (*$\Delta x = 0.1 cm$ *and* $\Delta t = 25 ms$*)*

never seen during experiments at the DeLight facility. In particular the manner in which the model is kept at a constant pressure by an in- and outflow of mass, is different from the experimental set-up. Moreover, the oscillations only occur at powers higher than the power that belongs to the maximum of the power-flow curve.

A possible scenario is that when an increase in power is supposed to result in a decrease in mass flow rate (according to the power-flow map above 5 kW, due to an increase in friction), oscillations of the mass flow rate (due to the power increase) result in an inaccurate prediction of the outflow of mass. For example, extra mass is drawn into the system when the part of the oscillation with a low temperature passes the 'buffer vessel'. But as the system is heating up, mass should have been removed from the system into the 'buffer vessel' instead. When these effects enhance each other, it can lead to the oscillations seen in figure 5.3. This seems to thus be a numerically driven oscillation.

In an effort to gain further understanding of this mechanism, the behaviour of the outflow of mass was studied. It was found that during steady state flow conditions the total outflow of mass was zero, but only as the result of a small outflow of mass at the beginning and an inflow of the same magnitude at the end of the section that allows

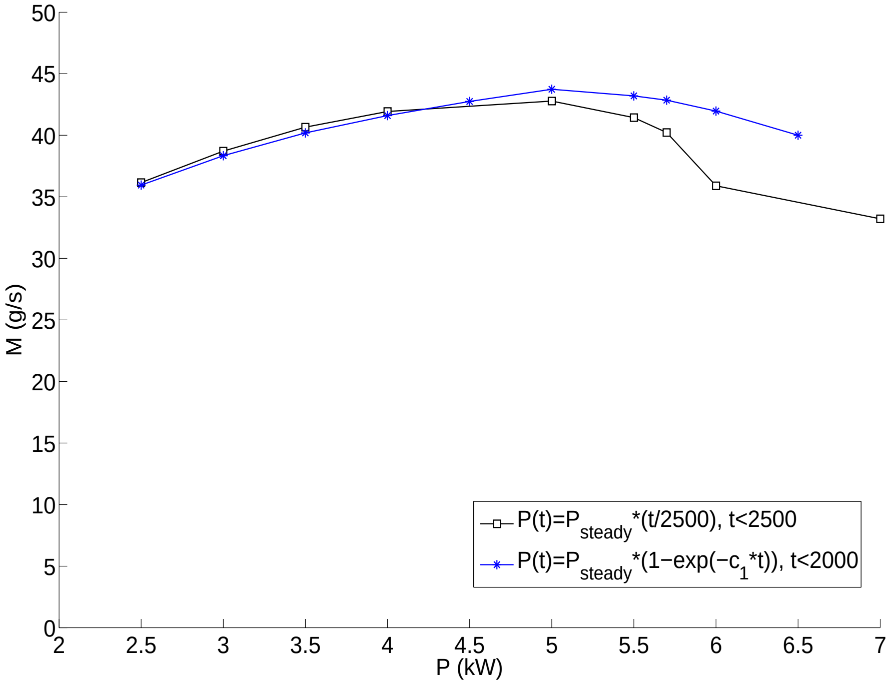

Figure 5.5: Comparison of power-flow maps generated with a linear increase in power and with an increase as described by equation 5.2. ($T_{in} = 0\,^0C$, $\Delta x = 0.1cm$ and $\Delta t = 25ms$)

in- and outflow of mass. First it was thought that a shift of this boundary could be the cause of the erratic oscillations, but the erratic oscillations were also seen with a modified outflow section where there was no mass inflow.

5.2 Convergence

To evaluate the performance of the code, it was subjected to a convergence test. For different time step (Δt) values, the program was run long enough to reach a steady state solution. Apart from the time, step all other parameters are kept constant. The same procedure is repeated for different grid spacings, Δx. The steady state mass flow rate that is obtained for a specific time step (or grid spacing), is normalized against the value obtained with the smallest time step (or grid spacing). Deviations in the mass flow rate for different temporal- and spatial grid sizes are expected to be largest, when the mass flow rate itself is maximal. For several time step and grid spacing sizes a power-flow curve was produced. For an inlet temperature of $0\,^0$C, a pressure of 57 bar and a HPLWR power distribution over the three core sections (53%, 30% and 17% in

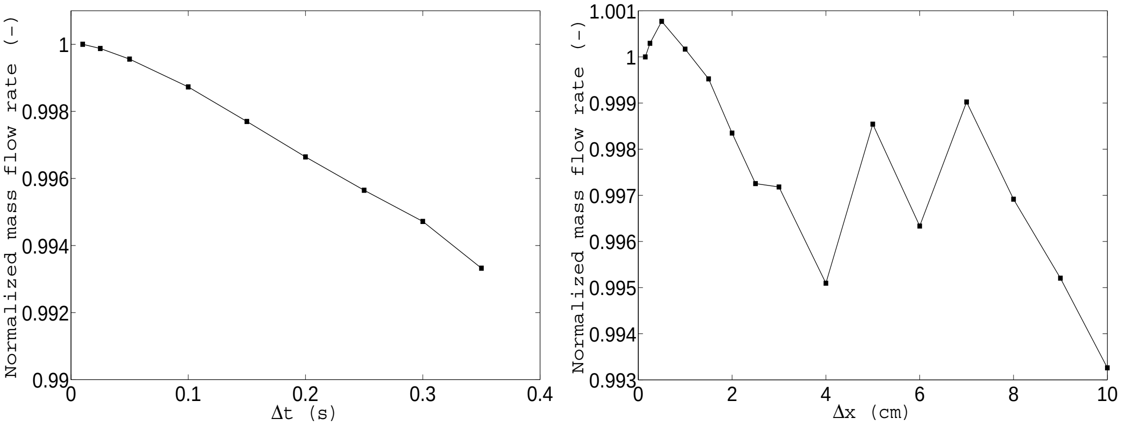

(a) *(b)*

Figure 5.6: Effect of grid refinement on the normalized mass flow rate, for varying time step values Δt, with $\Delta x = 2\,cm$ (a) and for varying mesh sizes Δx, with $\Delta t = 0.1\,s$ (b).

the direction of flow) the flow was found to be highest at a power of 5 kW. Therefore, the convergence test was carried out at P =5 kW and with the other parameters as mentioned above. The results of the convergence test are shown in figure 5.6.

As can be seen in figure 5.6(a), the mass flow rate hardly changes when Δt is smaller than 0.1 s, with $\Delta x = 2$ cm. The value of the steady state mass flow rate with $\Delta t = 0.1$ s is within 0.2% of the value obtained with $\Delta t = 0.01$ s. A time step size of 0.1 s was chosen based on these results. Decreasing the time step further results in much longer computational times, without large improvements in accuracy. The spatial grid refinement study depicted in figure 5.6(b) was subsequently performed with Δt =0.1 s and shows somewhat more irregular behaviour as the grid spacing is refined. An explanation might be given by the fact that all the different sections of the facility are separately divided into an integer number of nodes. As a result, there are possibly small variations in grid spacing throughout the system. Nonetheless, the solutions do seem to change little for grid spacings below 2.5 cm. As a result of the grid refinement study, a grid size of 1 cm and time step of 0.1 s will be used for the simulations that are carried out to investigate the stability of the system.

It is particularly important to verify that the crossover from stable to unstable (the stability threshold, where DR=1) and vice-versa, is independent of the grid size and time step used. Especially since the stability threshold of a one-dimensional system can be significantly overestimated if Δt and Δx are chosen too large, as shown by Jain and Rizwan-uddin (2008) for the supercritical CO_2 loop described earlier. The results of the decay ratio convergence tests will be presented using two non-dimensional numbers. The pseudo-subcooling number, N_{p-sub}, and the pseudo-phase change number, N_{p-pch}, with the pseudo-critical point as a reference condition (h_{pc}=288.03 kJ/Kg for R23 at 57 bar). These are derived in the scaling analysis by Rohde et al. (2011).

$$N_{p-pch} = \frac{P}{M_C h_{pc}} \tag{5.3}$$

$$N_{p-sub} = \frac{h_{pc} - h_{in}}{h_{pc}} \tag{5.4}$$

To investigate temporal- and spatial grid dependence of the decay ratio, an unstable point ($N_{p-sub} = 0.32$, N_{p-pch}=0.33) in the stability map (depicted in figure 5.8) of the DeLight facility was chosen. This stability map is the result of experiments carried out in October 2010 with a fuel constant of 6 s. The parameters of the point-kinetic model that were used during these experiments, differ from the parameters described in chapter 2 and are listed in table 5.2.

Table 5.2: Parameters of the point-kinetics model for DeLight used in the experiments of October 2010.

Fraction		Decay constant	
β_1	0.038β	λ_1	$0.0184\ \mathrm{s}^{-1}$
β_2	0.213β	λ_2	$0.046\ \mathrm{s}^{-1}$
β_3	0.188β	λ_3	$0.1668\ \mathrm{s}^{-1}$
β_4	0.407β	λ_4	$0.451\ \mathrm{s}^{-1}$
β_5	0.128β	λ_5	$2.0\ \mathrm{s}^{-1}$
β_6	0.026β	λ_6	$5.61\ \mathrm{s}^{-1}$
β	0.0065	Λ	$34.45\ \mu\mathrm{s}$

Special care is taken to use the same parameters when comparing experimental results with simulations. Furthermore, it is important to note that only simulations and experiments with the proper parameters (as listed in table 2.2) are valid as scaled results for the HPLWR.

For the (unstable) case mentioned above, convergence of the decay ratio was studied for different time step- and spatial grid sizes. The temporal- and spatial grid that resulted from the steady state mass flow rate analysis ($\Delta x = 1$ cm and $\Delta t = 0.1$ s) was found to be too coarse to simulate the stability of the DeLight facility with neutronic feedback. Simulations were carried out with Δx between 2 and 0.3 cm and Δt between 15 and 100 ms. These simulations show very little change of the decay ratios for the three smallest grids ($\Delta x = 0.3$ cm & $\Delta t = 25$ ms, $\Delta x = 1$ cm & $\Delta t = 25$ ms and $\Delta x = 1$ cm & $\Delta t = 15$ ms) as depicted in figure 5.7. It is important to note that to obtain accurate values for the decay ratio with neutronic feedback, the time step needs to be much smaller than was required for steady state solutions ($\Delta t = 25$ ms versus $\Delta t = 100$ ms).

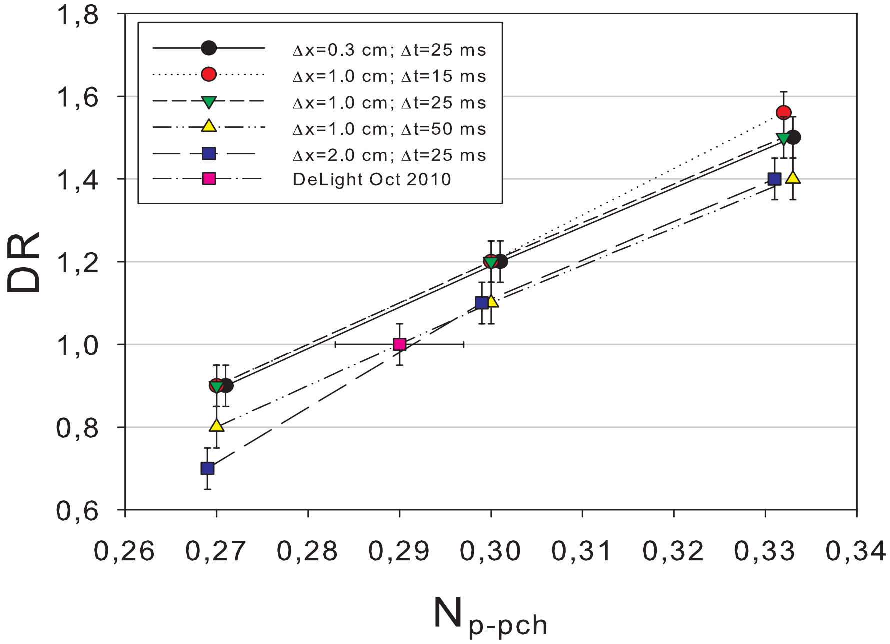

Figure 5.7: Grid refinement study to show grid independence of the stability threshold for $N_{p-sub} = 0.32$.

The effect of temporal- and spatial grid refinement on the decay ratio was investigated further by comparing several cases with the same pseudo-subcooling number, but with different pseudo-phasechange numbers. For a constant pseudo-subcooling number ($N_{p-sub} = 0.32$), the decay ratio is plotted against the pseudo-phase change number (N_{p-pch}) in figure 5.7.

Interpolation of the decay ratios in figure 5.7 show good convergence of the stability threshold for the temporal grid. However, the stability threshold is not independent of the spatial grid. Because the computational time needed to simulate a case with $\Delta x = 0.3\,\mathrm{cm}$ and $\Delta t = 25\,\mathrm{ms}$ is approximately 120 hours and a case with Δt=25 ms and Δx=1 cm is roughly ten times faster, further analysis of the stability boundary will be carried out with the latter grid size, as it seems to be sufficiently accurate to indicate the first stability threshold moving from small to large N_{p-pch}. It should also be pointed out that the time step of the neutronic feedback model in the experiments was the same. Interpolation of measured decay ratios at the DeLight facility result in a stability boundary ($DR = 1 \pm 0.05$) at $N_{p-pch} = 0.29 \pm 0.007$. Figure 5.7 shows good agreement of the experimental- and numerical stability threshold.

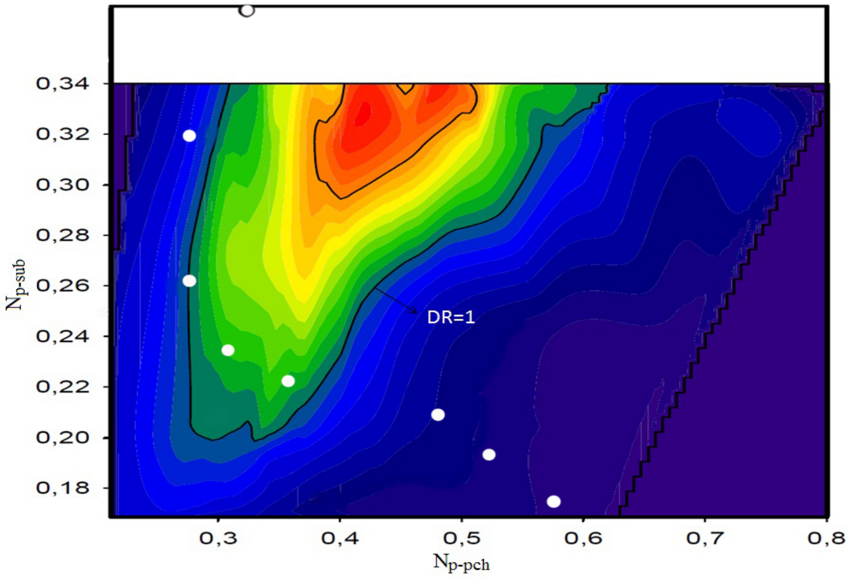

Figure 5.8: Comparison of the stability map from experiments on DeLight carried out in October 2010, with $\tau = 6\,s$ and neutronic feedback parameters as listed in table 5.2 and the stability threshold predicted by the code.

5.3 Experimental stability map

In October 2010, an experimental stability analysis of the DeLight facility was carried out. As was stated earlier, the parameters for the point-kinetic model of table 5.2 were used. The pressure was kept at approximately 57 bar and the fuel constant (τ) was set at 6 s, a typical value for a boiling water reactor. The stability map (in the N_{p-sub}-N_{p-pch} plane) that resulted from these experiments is depicted in figure 5.8.

This stability map is derived from the available experimental data through a third order fitting procedure. During an experiment the inlet temperature is kept constant and the decay ratio is measured for different power levels. The power step between different data points varied and was kept small near the stability threshold. Zones were no data was available are coloured in deep purple. In these zones the decay ratios were too small to measure (left top corner) or the power limit was reached (right bottom area). The set-up is also limited when it comes to inlet temperatures, and the maximum N_{p-sub} value is 0.34. The stability boundary (DR=1) is indicated in the graph. It can be seen that there is an unstable zone that becomes more unstable at lower inlet temperatures [T'Joen et al. (2011)].

The points marked by white symbols in figure 5.8 indicate the numerically predicted stability threshold. These points are determined through linear interpolation of the decay ratios between two N_{p-pch} values for a constant pseudo-subcooling number. The

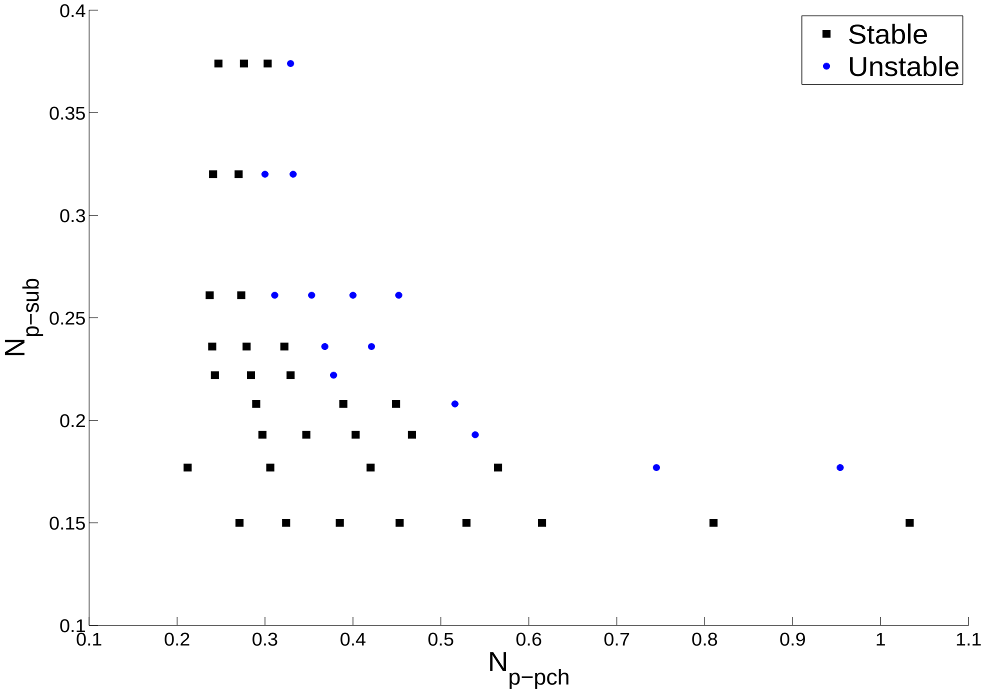

Figure 5.9: Stable and unstable data points in the N_{p-sub}-N_{p-pch} plane from the code.

available data points are depicted in figure 5.9. One stable point (with a decay ratio close to-, but smaller than one) and one unstable point (with a decay ratio larger than one) are used for a given inlet temperature.

As can be seen the agreement between the left boundary of the unstable zone and the numerically predicted stability threshold is very good, especially for high N_{p-sub} values. At low N_{p-sub} values (below 0.21), the code seems to underestimate stability, indicating a cross-over point where the experiments showed only stable operating conditions. It is unclear what is the cause; it could be due to the presence of a small preheating section in the downcomer to better control the inlet temperature which is not considered in the numerical simulations. The code is modified to consider the small preheating section in the downcomer. The simulations should be repeated with the proper heating in the downcomer to see if this can explain the difference. In section 5.4.3 the influence of the heating section in the downcomer is investigated for one subcooling number. The deviations can also be the result of differences between the geometry of the experimental set-up and the geometry described by the code. For example, the size and shape of the heat exchangers differ in the experimental set-up and the code.

Furthermore, it is interesting to note that the frequencies of the oscillations in the DeLight set-up were all approximately 0.1 Hz. The frequencies of the numerical oscillations, on the other hand, were approximately 0.1 Hz at the highest N_{p-sub} value, but the frequency increases for lower N_{p-sub} values, as can be seen in table 5.3. In section 2.3, it was already stated that Type-I instabilities in BWR's have small frequencies, just as was found for the first stability cross-over of DeLight in the experiments and numerically at high N_{p-sub} values. The higher frequencies of the instabilities at low N_{p-sub} values are typical for a transition to Type-II instabilities in a BWR.

Table 5.3: Frequencies of numerical oscillations at different N_{p-sub} values.

N_{p-sub}	0.374	0.261	0.222	0.208	0.177
$f(Hz)$	0.11	0.16	0.20	0.25	0.35

The impact of three parameters was studied experimentally [T'Joen et al. (2011)]. A smaller fuel time constant (2 s or 4 s instead of 6 s) reduced the size of the unstable area, shifting it up to the left top corner. Large fuel time constants in a BWR, have a stabilizing effect on Type-II oscillations, because of a filtering effect of high frequency oscillations in the void reactivity feedback loop. For Type-I oscillations the effect is opposite; large fuel time constants destabilize Type-I oscillations [Van Bragt (1998)]. Thus, the experimentally unstable zone seems to behave like a BWR Type-I region. An increased inlet friction resulted in a more stable system, with lower decay ratios. The most prominent effect was found for the power distribution. Changing the distribution to a uniform case (each core gives the same amount of power) made the system significantly more stable, shifting the unstable area to much higher N_{p-pch} values. These results are discussed in detail in the next section.

5.4 Parametric effects on stability

The stability characteristics of the DeLight facility are also investigated numerically. For different operating conditions and geometric parameters, the stability threshold is determined. All simulations are carried out with Δt=25 ms and Δx=1 cm at a pressure of 57 bar, with $N_{p-sub} = 0.32$ and $\tau = 6$ s (unless explicitly stated otherwise).

5.4.1 Effect of inlet- and outlet friction at the core

To study the effect of friction at the core in- and outlet, simulations were carried out with the system as depicted in figure A.1 in appendix A. A comparison is made between simulations without core in- and outlet friction and simulations with core inlet friction $K_{in} = 10$ at valve 1 and core outlet friction $K_{out} = 10$ at valve 4. The resulting

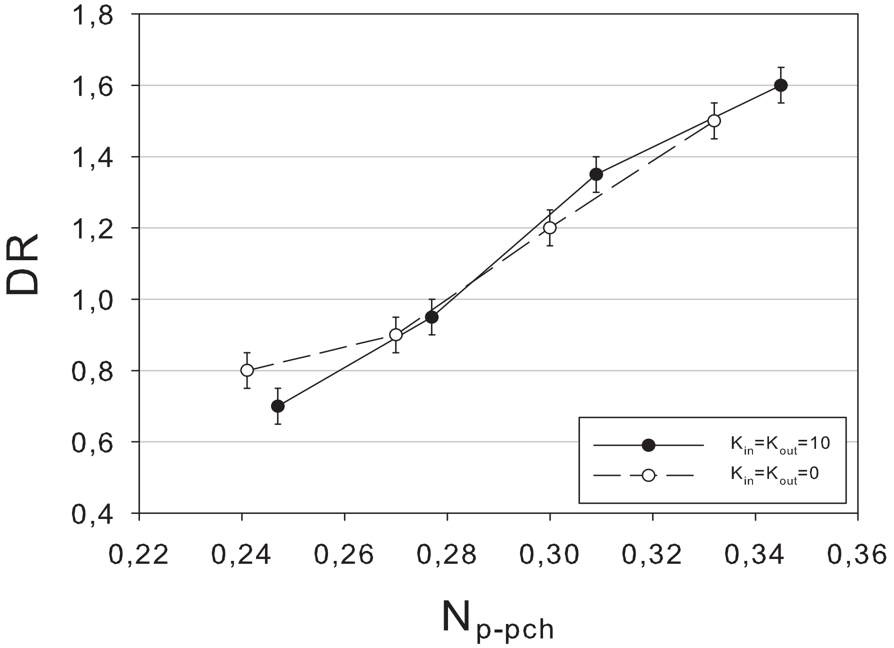

Figure 5.10: Comparison of decay ratios with and without in- and outlet friction in the core.

decay ratios are depicted in figure 5.10. Interpolation of the decay ratios results in a predicted stability boundary at $N_{p-pch} = 0.28 \pm 0.01$ for both systems. The in- and outlet friction don't influence the stability boundary of the system at $N_{p-sub} = 0.32$. Experiments on the DeLight facility, with different friction values at these valves, also showed no noticeable change of the stability threshold of the system. Only a decrease in experimental decay ratios at higher power was observed.

In a numerical study of the forced circulation HPLWR by Ortega Gomez (2009), it was found that (just as in a BWR) an increased inlet friction has a significantly stabilizing effect and an increased outlet friction has a destabilizing effect. The effects of the in- and outlet orifices were studied separately (either $K_{in} \neq 0$ or $K_{in} \neq 0$) by Ortega Gomez (2009).

5.4.2 Effect of a uniform power profile

As was stated earlier, the projected power distribution over the three core sections in the HPLWR design is 53%-30%-17%. To investigate the effect on the stability of the distribution, a comparison is made between simulations carried out with a uniform power profile and with the HPLWR power profile. As can be seen in figure 5.11 there is

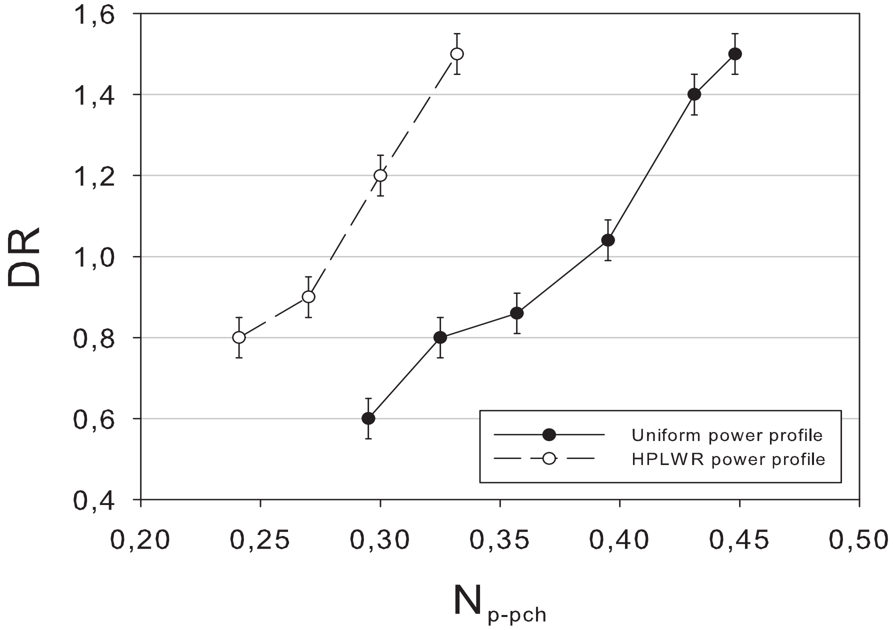

Figure 5.11: Comparison of decay ratios with HPLWR- and uniform power distribution.

a clear shift of the stability boundary. Interpolation of the decay ratios indicates that the stability threshold is moved from $N_{p-pch} = 0.28 \pm 0.01$ for the HPLWR distribution to $N_{p-pch} = 0.39 \pm 0.01$ for a uniform power distribution. Thus, the uniform power distribution results in a larger stable operating zone before the first stability boundary. This result was also seen experimentally, as was described in section 5.3. The larger stable operating zone might be a consequence of the density effect on the reactivity. For the HPLWR distribution the power perturbation is delivered predominantly on the first core section, whereas for the uniform distribution the power perturbation is spread out across all three core sections evenly. The higher stability for the uniform power profile can also be the result of the smaller density differences over the first core section, as this will definitely influence density oscillations. Similar results were found by Sanders (2009) for the forced circulation HPLWR.

A comparison of power-flow curves is given in figure 5.12 for both distributions and both stability boundaries are denoted by an arrow.

It can be seen that the uniform distribution leads to stable behaviour of the mass flow rate up to almost 5 kW, while the HPLWR distribution leads to unstable behaviour already at 3.2 kW. This indicates that using a ‘flatter’ power distribution positively influences the stability of the system, for low N_{p-pch} values. Because these simulations were not performed with the correct scaled down HPLWR reactivity parameters (as

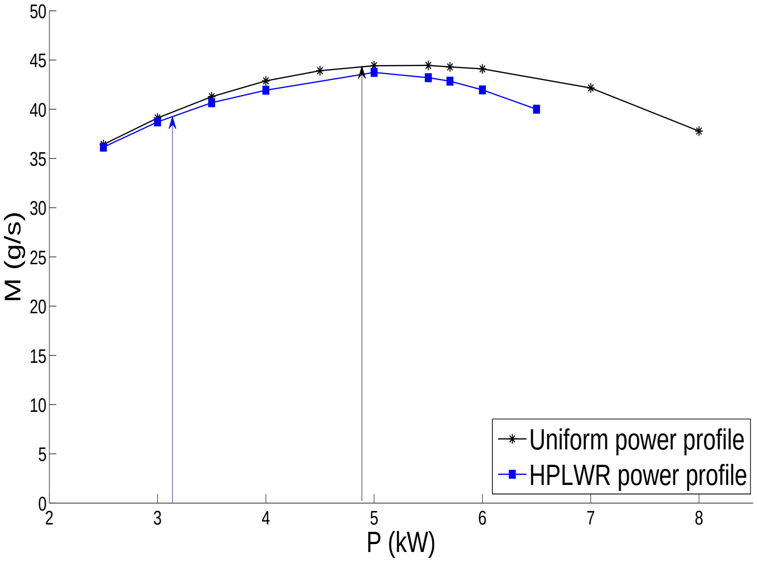

Figure 5.12: Comparison of power-flow maps for HPLWR- and uniform power distribution. The stability threshold is denoted by an arrow on both curves.

described in section 5.2), it is unsure whether these results are also applicable to the HPLWR. But if simulations with the right parameters lead to similar results, it might provide a valuable tool to increase the stability of the HPLWR during start-up.

It is also interesting to point out that the uniform power distribution results in a flatter power-flow curve. This flatter power-flow curve seems to positively influence the stability of the system described by the code during warm-up. The oscillations that were seen during warm-up with the HPLWR power distribution when the system was heated up too rapidly, only occurred with the uniform power distribution for powers well beyond the top of the power flow curve, at $P \approx 8\,\mathrm{kW}$. With the HPLWR distribution the oscillations can occur from $P \approx 5\,\mathrm{kW}$. It seems that these oscillations depend on the gradient of the power-flow curve. This supports the theory that the interplay between a necessary decrease in mass flow rate and the way that the pressure is kept constant, is the cause of difficulties in obtaining the correct steady state conditions at powers higher than the power that belongs to the top of the power-flow curve.

5.4.3 Effect of moderator rods

In the design of the HPLWR core, part of the water from the downcomer passes through special moderator rods in the fuel. It is inevitable that some heat will be transported from the fuel to the water that passes through these moderator rods (at nominal

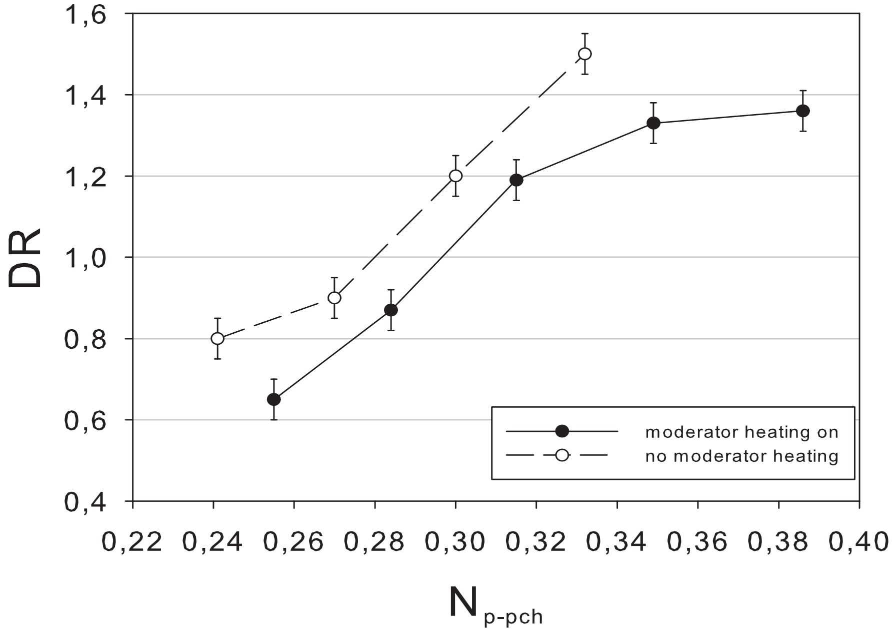

Figure 5.13: Comparison of decay ratios for core inlet temperature $T_{in} = 0\,^0C$, with and without heating at the moderator section in the downcomer. In the simulations with heating in the moderator section, the outlet temperature of the heat exchanger is set to -$10\,^0C$.

operating conditions, approximately 8% of the thermal power of the HPLWR core is delivered to the moderator water [Fisher et al. (2006)]). As a consequence, the water in these moderator rods will not have a constant density. This can influence the stability characteristics of the HPLWR. As was described in section 4.2, a heating section was added at the bottom of the downcomer in the DeLight facility, to investigate the effect these moderator rods might have on the stability.

In the model, it is also possible to heat the bottom section of the downcomer. At the beginning of the downcomer the coolant has a constant temperature equal to the specified exit temperature of the heat exchanger. In the last part of the downcomer (0.8 m), the coolant will be heated up to a specified core inlet temperature. Simulations were carried out with a coolant temperature after the heat exchanger of -10 ^{0}C. The coolant was then heated in the moderator section of the downcomer up to 0 ^{0}C before it entered the first core section. In figure 5.13, the decay ratios of these simulations are compared to those that were acquired without heating in the moderator section of the downcomer for the same core inlet temperature. The stability threshold of the 'moderated' case is predicted by interpolation of decay ratios at $N_{p-pch} = 0.30 \pm 0.01$.

For the case without heating in the moderator section this threshold is at $N_{p-pch} = 0.28 \pm 0.01$. This seems to be only a very minor change; negligible if uncertainties are taken into account. Since there is no neutronic-thermal hydraulic coupling in the moderator section described by the code and no transition of sub- to supercritical flow takes places, it is plausible that the stability characteristics are still dominated by the riser and the three core sections with neutronic feedback.

5.4.4 Effect of the fuel constant

To examine the influence of the fuel constant (τ) on the stability of the system, simulations are carried out for several realistic values (τ = 6, 4, 2 and 0.5 s). For a constant pseudo-subcooling number ($N_{p-sub} = 0.32$) the first stability threshold is determined by interpolation of decay ratios, moving from small to higher N_{p-pch} values. The numerical stability boundary is then compared to the stability boundary that was found during the experiments carried out in October 2010. The results are depicted in figure 5.14.

It was already shown in figure 5.8 that the numerically predicted stability threshold ($N_{p-pch} \approx 0.28$) is very close to the experimental value ($N_{p-pch} \approx 0.29$) for τ=6 s, at $N_{p-sub} = 0.32$. However, as the fuel constant is lowered to 4 s and 2 s it becomes clear that the numerical stability threshold and the experimental stability boundary deviate significantly.

During experiments the stability boundary shifted to higher N_{p-pch} numbers, for lower fuel constants, and the unstable zone in the N_{p-sub}-N_{p-pch} plane moved to higher N_{p-sub} values [T'Joen et al. (2011)]. The simulations at $N_{p-sub} = 0.32$, with lower fuel constants (τ =4 and 2 s) show a very minor shift of the stability threshold to a lower N_{p-pch} value ($N_{p-pch} \approx 0.26$) and the stability threshold moves back again to a somewhat higher pseudo phase change number ($N_{p-pch} \approx 0.27$) for simulations with an even smaller fuel constant (τ =0.5 s).

It is interesting to point out that large fuel time constants have a destabilizing effect on Type-I oscillations in a natural circulation BWR. On Type-II oscillations, on the other hand, large fuel time constants have a stabilizing effect [Van Bragt (1998)]. Because of the many similarities between BWR's and SCWR's, it is expected that both instability types also occur in SCWR's. It can be said that the unstable zone from the experimental results at the DeLight facility does behave like a Type-I unstable zone. However, the first stability threshold, moving from low to high phasechange numbers in a BWR, is fixed at $N_{sub} = N_{pch}$ [Van Bragt (1998)], while the first stability threshold in the DeLight facility changed significantly in the experiments. The numerically predicted first stability cross-over, however, varies very little as the fuel constant is changed.

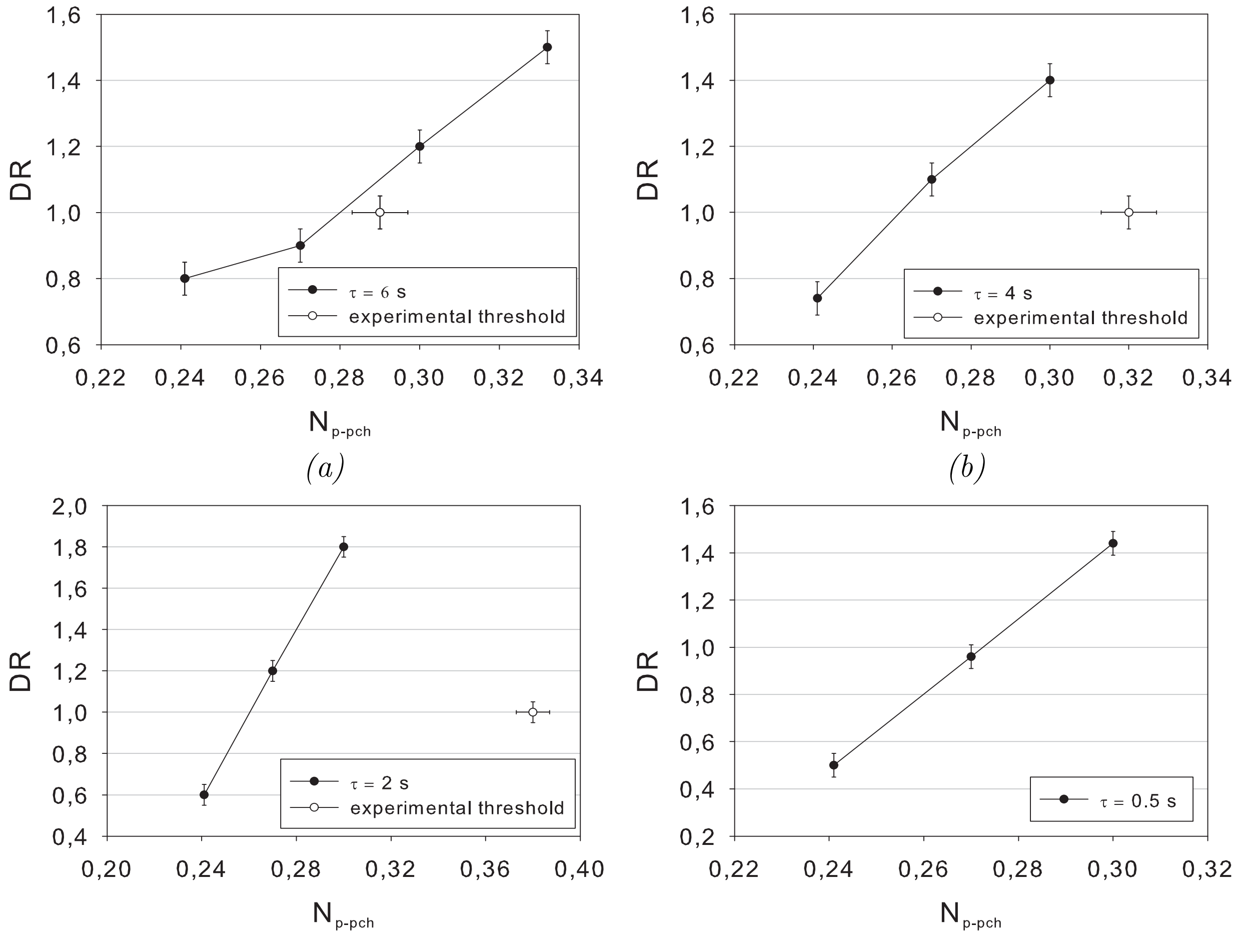

(a) *(b)*

(c) *(d)*

Figure 5.14: Comparison of numerical and experimental stability threshold for different fuel constants.

The large difference between the experimental and numerical results for lower fuel constants (at $N_{p-sub} = 0.32$) might have the same origin as the difference that occurs for lower N_{p-sub} with $\tau = 6$ s (see figure 5.8). The uncertainty in the stability boundary at the bottom of the experimentally unstable zone is larger, as a slight deviation between experimental and numerical operating conditions results in a large error of the predicted stability boundary in this region. Since this zone moved upwards for lower fuel constants [T'Joen et al. (2011)], the range of pseudo-subcooling numbers for which the stability threshold prediction by the code is accurate, might have been shifted upward as well.

Chapter 6

Conclusions & Outlook

6.1 Conclusions

A code was developed to investigate the coupled thermal hydraulic-neutronic stability of a scaled facility mimicking the physics of a natural circulation SCWR. A power-flow map produced with the code for a supercritical CO_2 loop found in literature showed very good agreement (deviations between 0.6 and 1.2%). For the DeLight facility (scaled from the natural circulation HPLWR) a power-flow map generated by the code was compared to data from the experimental set-up. The code predicted the steady state mass flow rate within 4% of the measured value over the investigated range of powers (3-8 kW). The discretized system of equations and the mechanism that is used to solve these equations is deemed adequate to predict steady state mass flow rates. Nonetheless, simulations should always be checked for the presence of erratic oscillations as described in section 5.1.3.

The dynamic behaviour of the mass flow rate after a perturbation was also investigated. A temporal- and spatial grid refinement study of the stability threshold was performed for low N_{p-pch} values at one N_{p-sub} value (0.32). The resulting grid ($\Delta t = 25\,\text{ms}$ and $\Delta x = 0.1\,\text{cm}$) is used for further investigation of the stability with the code.

Experimental stability measurements with one fuel constant ($\tau = 6\,\text{s}$) are compared to simulations for several inlet temperatures and over a range of powers. The left boundary of an experimentally unstable zone in the N_{p-sub}-N_{p-pch} plane was successfully predicted by simulations for high N_{p-sub} values. At low N_{p-sub} and high N_{p-pch} values however, the code indicated a cross-over point where the experiments showed only stable operating conditions. The frequencies of these instabilities indicate a transition of Type-I and Type-II oscillations, just as in a natural circulation BWR [Van Bragt (1998)]. Furthermore, a numerical parameter study was performed and the results are compared to data from experimental parameter studies when available.

A study regarding parametric effects was carried out for one N_{p-sub} value (0.32). It was found that increasing in- and outlet friction didn't influence the stability threshold for low N_{p-pch} values. Experiments yielded similar results. Heating in the bottom section of the downcomer (modelling the moderator rods in the HPLWR core) resulted in a very minor shift of the stability boundary, towards higher N_{p-pch} values. Lowering the fuel constant (τ) resulted experimentally in a shift of the unstable zone in the N_{p-sub}-N_{p-pch} plane towards higher N_{p-sub} values. Numerically this result wasn't seen for $N_{p-sub} = 0.32$; at this N_{p-sub} value the numerically predicted stability threshold moved away from the experimental stability threshold for lower τ values. It is unclear what causes these differences.

The most significant influence on the stability was both experimentally and numerically found for the power distribution. Changing the power profile from the HPLWR distribution to a uniform profile resulted in a large shift of the stability boundary towards higher N_{p-pch} values. Hence, the system is considerably more stable, at low N_{p-pch} values, with a uniform power distribution.

6.2 Outlook

It is recommended to perform a temporal- and spatial grid refinement study around the cross-over point from the experimentally unstable- to the experimentally stable zone at high N_{p-pch} values for $\tau = 6\,\mathrm{s}$. As a consequence, the stability of a larger part of the N_{p-sub}-N_{p-pch} plane could be investigated numerically. It is even expected that a third stability threshold can be found, as the stable zone at high N_{p-pch} values crosses over to an unstable zone, like the Type-II instability zone in a BWR described by Van Bragt (1998).

Furthermore, it would be very interesting to see the effects of the parameter study for several N_{p-sub} values in the N_{p-sub}-N_{p-pch} plane, as this would provide more information about the zone in the plane where the code is accurate or not. Especially the magnitude of the numerically and experimentally different effects of a lower fuel constant could be enlightened by simulations over a wide range of N_{p-sub} and N_{p-pch} values. Investigation of the separate effect of an increased in- and outlet friction can also be recommended, as well as an investigation into the effect of a change in geometry, for example the riserlength.

Since all simulations so far aren't carried out with the HPLWR neutronic parameters, the results are not valid as scaled results from the HPLWR. Therefore it is also recommended to repeat the stability analysis with the proper neutronic parameters.

It might be worthwhile to look into different convergence criteria for the solution algorithm, other than just monitoring the pressure. Also the influence of the in- and outflow of mass on the stability can be investigated further, for example by not allowing any in- and outflow of mass after the steady state mass flow rate is reached (this is already successfully implemented in a test-version of the code).

By eliminating calls to the NIST [Huber et al. (2002)] properties package (for temperature and partial derivatives of the density) and replacing them with splines (as was done for the viscosity), the computational time can be reduced significantly. However, it is unsure whether or not this will create numerical instabilities as was reported by Koopman (2008). These numerical instabilities were probably also seen during early stability simulations with the supercritical CO_2 loop. Therefore special care must be taken to validate simulations with the recommended changes, with the results described in this thesis.

Appendix A

Flow obstruction constants

The friction coefficient, K_i, for turbulent flow through tube systems is described elaborately by Janssen and Warmoeskerken (2006). The values of the friction coefficients used in the simulations are described in table A. If other coefficients are used for parametric studies, it will be stated explicitly. The locations of the obstacles represented by these coefficients are depicted in figure A.1

Table A: Friction coefficients.

description	K_i
smooth bend 90^0	0.13
smooth bend 1	0.17
smooth bend 2	0.09
gradual contraction	0.0
gradual enlargement	0.0
valve 1	0.0
valve 2	0.0
valve 3	0.0
valve 4	0.0
valve 5	0.0

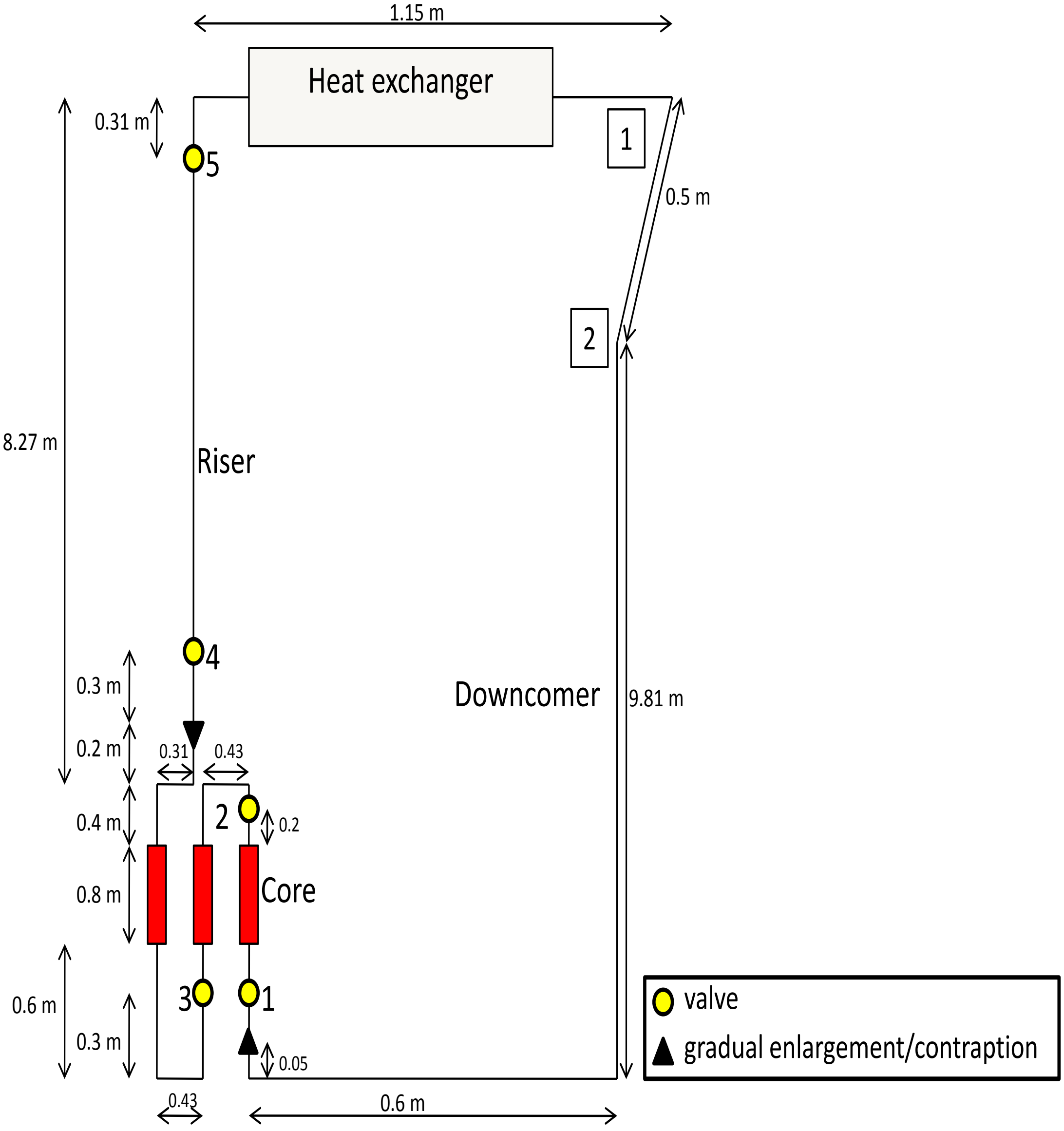
1.15 m
Heat exchanger
0.31 m
5
1
0.5 m
2
8.27 m
Riser
4
Downcomer
9.81 m
0.3 m
0.2 m
0.31
0.43
0.4 m
2
0.2
0.8 m
Core
0.6 m
0.3 m
3
1
0.05
0.43
0.6 m
valve
gradual enlargement/contraption

Figure A.1: Schematic representation of the geometry used in the code. Bends other than 1 and 2 are 90^0*, for all bends radius/diameter=5. The tube inner diameter is* $6\,mm$ *in the core section between the contraption and the enlargement, elsewhere it is* $10\,mm$*. The length of the contraption/enlargement is* $3\,cm$*.*

Appendix B

Scaling factors

The HPLWR can be scaled down to an experimental facility with the scaling rules provided in Rohde et al. (2011) in such a way that the physics involved is the same for both systems.

A scaling factor, X_q, that scales a quantity, q, in the HPLWR to the same quantity in the DeLight facility is defined as follows:

$$X_q = \frac{q_{DeLight}}{q_{HPLWR}} \tag{B.1}$$

Some of the different scaling factors derived in Rohde et al. (2011) are listed in table B. With the density scaling factor and a little algebra it is possible to deduce the scaling factor for the density coefficient of reactivity.

Table B: Scaling factors from HPLWR to DeLight.

property	symbol	value
axial length	X_L	0.191
time	X_t	0.438
hydraulic diameter	X_D	1.06
flow area	X_A	0.794
power	X_P	0.0788
density	X_ρ	1.69

Since the reactivity is equal for both systems, equation 2.30 is also equal for both systems:

$$\alpha_{\rho_{coolant,HPLWR}} \delta\rho_{coolant,HPLWR} = \alpha_{\rho_{coolant,DeLight}} \delta\rho_{coolant,DeLight} \tag{B.2}$$

This can be rewritten as:

$$\alpha_{\rho_{coolant},DeLight} = \alpha_{\rho_{coolant,HPLWR}} \frac{\delta\rho_{coolant,HPLWR}}{\delta\rho_{coolant,DeLight}} \tag{B.3}$$

So the scaling factor for the density coefficient of reactivity is:

$$\begin{aligned} X_{\alpha_{\rho_{coolant}}} &= \frac{\delta\rho_{coolant,HPLWR}}{\delta\rho_{coolant,DeLight}} \\ &= \frac{\rho_{coolant,HPLWR} - \bar{\rho}_{coolant,HPLWR}}{\rho_{coolant,DeLight} - \bar{\rho}_{coolant,DeLight}} \\ &= \frac{\rho_{coolant,HPLWR} - \bar{\rho}_{coolant,HPLWR}}{\left(\rho_{coolant,HPLWR} - \bar{\rho}_{coolant,HPLWR}\right) X_{\rho}} \end{aligned} \tag{B.4}$$

Which can be simplified to:

$$X_{\alpha_{\rho_{coolant}}} = \frac{1}{X_{\rho}} \tag{B.5}$$

List of Figures

1.1 A simplified illustration of the DeLight facility. 3

2.1 Concentration of data points at pseudo critical point to capture the sharp change in viscosity. 8

2.2 A schematic representation of fission of uranium-235 and moderation of neutrons. [figure from Ortega Gomez (2009)] 10

2.3 A schematic representation of the coolant density feedback mechanism. 12

2.4 Illustration of the local pressure drop delay introduced by the density wave mechanism. [figure revision from March-Leuba and Rey (1993)] . 16

2.5 Examples of a stable (a) and unstable (b) mass flow rate at the core inlet. 17

3.1 Discretization grid. 20

3.2 Schematic drawing of the top of the one dimensional loop, in order to depict the position of the heat exchanger, the enthalpy drain and the nodes where the enthalpy is set to the desired inlet enthalpy. 23

4.1 A schematic representation of the DeLight facility [Figure from T'Joen et al. (2011)]. 30

5.1 Schematic representation of the supercritical CO_2 loop described by Jain and Rizwan-uddin (2008) and comparison of power-flow maps. Results are generated with Δx=0.2 cm and Δt=0.35 s using the own code. . . . 36

5.2 Power-flow maps from the DeLight facility and the code generated with $\Delta x = 0.5$cm and $\Delta t = 0.1$s to validate the friction multiplication factor in the modelled heat exchanger. 38

5.3 Growing oscillations of the mass flow rate at the core inlet (a) and erratic decay of the oscillations with a different frequency (b) leading to an inaccurate steady state solution for $P = 5.7\,\mathrm{kW}$, $T_{in} = 0\,^0\mathrm{C}$, $\Delta x = 0.1\mathrm{cm}$ and $\Delta t = 25\mathrm{ms}$ at 57 bar. 39

5.4 Warm-up period of 2000 s to reach steady state solution for $P = 5.7\,\mathrm{kW}$ and $T_{in} = 0\,^0\mathrm{C}$ at 57 bar with equation 5.2. ($\Delta x = 0.1\mathrm{cm}$ and $\Delta t = 25\mathrm{ms}$) 40

5.5 Comparison of power-flow maps generated with a linear increase in power and with an increase as described by equation 5.2. ($T_{in} = 0\,^0\mathrm{C}$, $\Delta x = 0.1\mathrm{cm}$ and $\Delta t = 25\mathrm{ms}$) 41

5.6 Effect of grid refinement on the normalized mass flow rate, for varying time step values Δt, with $\Delta x = 2\,\mathrm{cm}$ (a) and for varying mesh sizes Δx, with $\Delta t = 0.1\,\mathrm{s}$ (b). 42

5.7 Grid refinement study to show grid independence of the stability threshold for $N_{p-sub} = 0.32$. 44

5.8 Comparison of the stability map from experiments on DeLight carried out in October 2010, with $\tau = 6\,\mathrm{s}$ and neutronic feedback parameters as listed in table 5.2 and the stability threshold predicted by the code. . . 45

5.9 Stable and unstable data points in the N_{p-sub}-N_{p-pch} plane from the code. 46

5.10 Comparison of decay ratios with and without in- and outlet friction in the core. 48

5.11 Comparison of decay ratios with HPLWR- and uniform power distribution. 49

5.12 Comparison of power-flow maps for HPLWR- and uniform power distribution. The stability threshold is denoted by an arrow on both curves. 50

5.13 Comparison of decay ratios for core inlet temperature $T_{in} = 0\,^0\mathrm{C}$, with and without heating at the moderator section in the downcomer. In the simulations with heating in the moderator section, the outlet temperature of the heat exchanger is set to -10 ^{0}C. 51

5.14 Comparison of numerical and experimental stability threshold for different fuel constants. 53

A.1 Schematic representation of the geometry used in the code. Bends other than 1 and 2 are 90^0, for all bends radius/diameter=5. The tube inner diameter is $6\,mm$ in the core section between the contraption and the enlargement, elsewhere it is $10\,mm$. The length of the contraption/enlargement is $3\,cm$. 60

Bibliography

Bijl, H., 1999, Computation of flow at all speeds with a staggered scheme: Ph.D. thesis, Delft University of Technology.

Boure, J., Bergles, A., and Tong, L. S., 1973, Review of two-phase flow instability: *Nuclear Engineering and Design*, **25**, no. 1, 165–192.

Duderstadt, J. J., and Hamilton, L. J., 1976, *Nuclear Reactor Analysis*: John Wiley & Sons.

Fisher, K., Starflinger, J., and Schulenberg, T., 2006, Conceptual design of a reactor pressure vessel and its internals for a HPLWR: *Nuclear Engineering and Design*, , no. ICAPP 06, Reno, United States, June 4-8, Paper No. 6098.

Fisher, K., Schulenberg, T., and Laurien, E., 2009, Design of a supercritical water-cooled reactor with a three-pass core arrangement: *Nuclear Engineering and Design*, **239**, 800–812.

Haaland, S. E., 1983, Simple and explicit formulas for the friction factor in turbulent pipe flow: *Journal of Fluids Engineering(ASME)*, **105**, no. 1, 89–90.

Holmes, M. H., 1999, Tridiagonal solver: *http://www.rpi.edu/h̃olmes/NumDiffEqs/Demos/TridiagonalSolver.pdf*.

Huber, M. L., Lemmon, E. W., and McLinden, M. O., 2002, NIST Reference fluid thermodynamic and transport properties-REFPROP: *U.S. Department of Commerce, Technology Administration*, **version 7.0**.

Jain, P. K., and Rizwan-uddin, 2008, Numerical analysis of supercritical flow instabilities in a natural circulation loop: *Nuclear Engineering and Design*, **238**, 1947–1957.

Janssen, L. P. B. M., and Warmoeskerken, M. M. C. G., 2006, *Physical Transport Phenomena Data Companion, third edition*: VSSD.

Kazimi, M. S., and Todreas, N. E., 1990, *Nuclear Systems I: Thermal Hydraulic Fundamentals*: Taylor & Francis.

Koopman, H. K., 2008, Development of the STEALTH-code and investigation of the effects of feedwater sparger positioning on the thermal-hydraulic stability of natural circulation boiling water reactors: Masters's thesis, Delft University of Technology.

Marcel, C. P., 2007, Experimental and Numerical Stability investigations on Natural Circulation Boiling Water Reactors: Ph.D. thesis, Delft University of Technology.

March-Leuba, J., and Rey, J. M., 1993, Reactivity Control Mechanisms for a HPLWR Fuel Assembly: *Nuclear Engineering and Design*, **145**, 97–111.

Oppenheim, A. V., and Willsky, A. S., 1997, *Signals & Systems, second edition*: Prentice-Hall, Inc.

Ortega Gomez, T., 2009, Stability Analysis of the High Performance Light Water Reactor: Ph.D. thesis, Forschungszentrum Karlsruhe, Institute for Nuclear and Energy Technologies, University of Karlsruhe.

Press, W. H., Teukolsky, S. A., Vetterling, W. T., and Flannery, B. P., 1992, *Numerical Recipes in C: the art of scientific computing*: Cambridge University Press.

Rohde, M., Marcel, C. P., T'Joen, C., and Van der Hagen, T. H. J. J., 2011, Downscaling a supercritical water loop for experimental studies on system stability: *International Journal of Heat and Mass Transfer*, **54**, no. 1-3, 65–74.

Rohde, M., 2010, *Implementation of the VRF system in DeLight*: Internal report.

Sanders, M. B., 2009, Thermo-hydraulic stability analysis of the High Performance Light Water Reactor and a scaled experimental facility: Masters's thesis, Delft University of Technology.

Schlagenhaufer, M., Vogt, B., and Schulenberg, T., 2007, Reactivity Control Mechanisms for a HPLWR Fuel Assembly: *Global 2007*, pages 934–943.

Schulenberg, T., Starflinger, J., and Heinecke, J., 2008, Three pass core design proposal for a high performance light water reactor: *Progress in Nuclear Energy*, **50**, no. 2-6, 526–531.

Stewart, J., 1999, *Calculus, early transcendentals, fourth edition*: Brooks/Cole Publishing Company.

T'Joen, C., Kam, F., and Rohde, M., 2011, Stability research on a natural circulation driven SCWR: NURETH 14, Toronto, Ontario, Canada.

Van Bragt, D. D. B., 1998, Analytical Modeling of Boiling Water Reactor Dynamics: Ph.D. thesis, Delft University of Technology.

Van der Hagen, T. H. J. J., 1988, Experimental and theoretical evidence for a short effective fuel time constant in a boiling water reactor: *Nuclear Technology*, **83**, no. 2, 171–181.

Wesseling, P., Zijlema, M., and Segal, A., 1995, Finite volume computation of incompressible turbulent flows in general coordinates on staggered grids: *International Journal for Numerical Methods in Fluids*, **20**, 621–640.

Nomenclature

Symbol	Dimension	Description
b	-	constant
c	-	warm-up time constant
f	-	friction factor
f	Hz	frequency
$f_{fr,HX}$	-	multiplication factor in heat exchanger
g	$\mathrm{m\,s^{-2}}$	gravitational acceleration
g_f	-	transfer function in time domain
h	$\mathrm{J\,kg^{-1}}$	specific enthalpy
k	-	multiplication factor
l	s	prompt neutron lifetime
n	neutrons per $\mathrm{m^3}$	neutron density
$\underline{n}'$	-	relative neutron density perturbation
p	Pa	pressure
$\underline{p}'$	-	relative power perturbation q'
$\mathrm{W\,m^{-1}}$	linear heating rate	
q'''	$\mathrm{W\,m^{-3}}$	volumetric heat generation
t	s	time
Δt	s	time step
u	$\mathrm{J\,kg^{-1}}$	specific internal energy
v	$\mathrm{m\,s^{-1}}$	velocity
w_f	J per event	energy released per fission event
x	m	coordinate in one-dimensional space
Δx	m	grid size
A	$\mathrm{m^2}$	cross-sectional area
C_i	$\mathrm{m^{-3}}$	delayed neutron precursor concentration
D	m	diameter
D_h	m	hydraulic diameter
DR	-	decay ratio
F	-	proportionality factor
G_F	-	transfer function in z-domain
H	J	enthalpy
H_{step}	-	Heaviside step function

Symbol	Dimension	Description
K	-	friction constant
L	m	length
M	$\mathrm{kg\,s^{-1}}$	mass flow rate
N_{p-pch}	$\frac{P}{M_C h_{pc}}$	pseudo phase change number
N_{p-sub}	$\frac{h_{pc}-h_{in}}{h_{pc}}$	pseudo suboooling number
N	-	total number of nodes
$\underline{N}'$	-	corrected relative neutron density perturbation
P	W	power
P_w	m	wetted perimeter
Q	W	internal heat production
Re	$\frac{\rho\|\vec{v}\|D_h}{\mu}$	Reynold's number
T	K	temperature
V	$\mathrm{m^3}$	volume
X	-	scaling constant
Greek		
α	-	coefficient of reactivity
α	-	void fraction
β	-	delayed precursor fraction
χ	-	quality
δ	-	change
ϵ	m	wall roughness
γ	-	Sherman-Morrison parameter
λ	$\mathrm{s^{-1}}$	decay constant
μ	$\mathrm{Pa\,s}$	dynamic viscosity
ρ	$\mathrm{kg\,m^{-3}}$	density
ρ	-	reactivity
τ	s	fuel time constant
τ_w	$\mathrm{kg\,m^{-1}\,s^{-2}}$	wall friction
Φ	$\mathrm{m^{-2}\,s^{-1}}$	neutron flux
Λ_{gen}	s	mean lifetime of neutron generation
Σ_f	$\mathrm{m^{-1}}$	macroscopic cross-secction for fission
Ψ	-	spatial dependence of neutron flux
subscripts		
coolant	-	property of the coolant
cooled	-	cooled part
ext	-	external
extra	-	resulting from reactivity feedback
heated	-	heated part

Symbol	Dimension	Description
i	-	delayed precursor group number
i	-	position in the grid
j	-	node in the grid
n	-	neutron
out	-	out of the system
pc	-	pseudo critical
$reactivity$	-	reactivity property
sys	-	system
w	-	wall
x	-	in the x-direction
C	-	core
HX	-	heat exchanger
α	-	coefficient of reactivity property
ρ	-	density property
0	-	steady state value
superscripts		
k	-	iteration value
n	-	time step
0	-	stagnation
$*$	-	initial guess
$'$	-	correction
$'$	-	perturbation